The importance of cellular-scale viral dynamics in bat reservoirs for emerging zoonotic disease

Cara E. Brook[1,2†], Mike Boots[1], Kartik Chandran[3], Andrew P. Dobson[2], Christian Drosten[4], Andrea L. Graham[2], Bryan T. Grenfell[2,5], Marcel A. Müller[4,6], Melinda Ng[3], Lin-Fa Wang[7], Anieke van Leeuwen[8,2]

[1] Department of Integrative Biology, University of California, Berkeley, Berkeley, CA, USA.

[2] Department of Ecology & Evolutionary Biology, Princeton University, Princeton, NJ, USA.

[3] Department of Microbiology and Immunology, Albert Einstein College of Medicine, Bronx, NY, USA.

[4] Institute of Virology, Charité-Universitätsmedizin Berlin, corporate member of Freie Universität Berlin, Humboldt-Universität zu Berlin, and Berlin Institute of Health, Berlin, Germany.

[5] Fogarty International Center, National Institutes of Health, Bethesda, Maryland, USA.

[6] Martsinovsky Institute of Medical Parasitology, Tropical and Vector Borne Diseases, Sechenov University, Moscow, Russia.

[7] Emerging Infectious Diseases Program, Duke-National University of Singapore Medical School, Singapore.

[8] Royal Netherlands Institute for Sea Research, Department of Coastal Systems, and Utrecht University, the Netherlands

Abstract

Bats host virulent zoonotic viruses without experiencing disease. A mechanistic understanding of the impact of bats' virus hosting capacities, including uniquely constitutive immune pathways, on cellular-scale viral dynamics is needed to elucidate zoonotic emergence. We carried out virus infectivity assays on bat cell lines expressing induced and constitutive immune phenotypes, then developed a theoretical model of our *in vitro* system, which we fit to empirical data. Best fit models recapitulated expected immune phenotypes for representative cell lines, supporting robust antiviral defenses in bat cells that correlated with higher estimates for within-host viral propagation rates. In general, heightened immune responses limit pathogen-induced cellular morbidity to promote the establishment of rapidly-propagating persistent infections within-host. Rapidly-replicating viruses that have evolved with bat immune systems will likely cause enhanced virulence following emergence into secondary hosts with immune systems that diverge from those unique to bats.

47 **Introduction**

48 Bats have received much attention in recent years for their role as reservoir hosts for
49 emerging viral zoonoses, including rabies and related lyssaviruses, Hendra and Nipah
50 henipaviruses, Ebola and Marburg filoviruses, and SARS coronavirus (Calisher et al. 2006;
51 Wang and Anderson 2019). In most non-Chiropteran mammals, henipaviruses, filoviruses, and
52 coronaviruses induce substantial morbidity and mortality, display short durations of infection,
53 and elicit robust, long-term immunity in hosts surviving infection (Nicholls et al. 2003; Hooper
54 et al. 2001; Mahanty and Bray 2004). Bats, by contrast, demonstrate no obvious disease
55 symptoms upon infection with pathogens that are highly virulent in non-volant mammals
56 (Schountz et al. 2017) but may, instead, support viruses as long-term persistent infections, rather
57 than transient, immunizing pathologies (Plowright et al. 2016).

58 Recent research advances are beginning to shed light on the molecular mechanisms by
59 which bats avoid pathology from these otherwise virulent pathogens (Brook and Dobson 2015).
60 Bats leverage a suite of species-specific mechanisms to limit viral load, which include host
61 receptor sequence incompatibilities for some bat-virus combinations (Ng et al. 2015) and
62 constitutive expression of the antiviral cytokine, IFN-α, for others (Zhou et al. 2016). Typically,
63 the presence of viral RNA or DNA in the cytoplasm of mammalian cells will induce secretion of
64 type I interferon proteins (IFN-α and IFN-β), which promote expression and translation of
65 interferon-stimulated genes (ISGs) in neighboring cells and render them effectively antiviral
66 (Stetson and Medzhitov 2006). In some bat cells, the transcriptomic blueprints for this IFN
67 response are expressed constitutively, even in the absence of stimulation by viral RNA or DNA
68 (Zhou et al. 2016). In non-flying mammals, constitutive IFN expression would likely elicit
69 widespread inflammation and concomitant immunopathology upon viral infection, but bats

support unique adaptations to combat inflammation (Zhang et al. 2013; Ahn et al. 2019; Xie et al. 2018; Pavlovich et al. 2018) that may have evolved to mitigate metabolic damage induced during flight (Kacprzyk et al. 2017). The extent to which constitutive IFN-α expression signifies constitutive antiviral defense in the form of functional IFN-α protein remains unresolved. In bat cells constitutively expressing IFN-α, some protein-stimulated, downstream ISGs appear to be also constitutively expressed, but additional ISG induction is nonetheless possible following viral challenge and stimulation of IFN-β (Zhou et al. 2016; Xie et al. 2018). Despite recent advances in molecular understanding of bat viral tolerance, the consequences of this unique bat immunity on within-host virus dynamics—and its implications for understanding zoonotic emergence—have yet to be elucidated.

The field of 'virus dynamics' was first developed to describe the mechanistic underpinnings of long-term patterns of steady-state viral load exhibited by patients in chronic phase infections with HIV, who appeared to produce and clear virus at equivalent rates (Nowak and May 2000; Ho et al. 1995). Models of simple target cell depletion, in which viral load is dictated by a bottom-up resource supply of infection-susceptible host cells, were first developed for HIV (Perelson 2002) but have since been applied to other chronic infections, including hepatitis-C virus (Neumann et al. 1998), hepatitis-B virus (Nowak et al. 1996) and cytomegalovirus (Emery et al. 1999). Recent work has adopted similar techniques to model the within-host dynamics of acute infections, such as influenza A and measles, inspiring debate over the extent to which explicit modeling of top-down immune control can improve inference beyond the basic resource limitation assumptions of the target cell model (Baccam et al. 2006; Pawelek et al. 2012; Saenz et al. 2010; Morris et al. 2018).

92 To investigate the impact of unique bat immune processes on *in vitro* viral kinetics, we
93 first undertook a series of virus infection experiments on bat cell lines expressing divergent
94 interferon phenotypes, then developed a theoretical model elucidating the dynamics of within-
95 host viral spread. We evaluated our theoretical model analytically independent of the data, then
96 fit the model to data recovered from *in vitro* experimental trials in order to estimate rates of
97 within-host virus transmission and cellular progression to antiviral status under diverse
98 assumptions of absent, induced, and constitutive immunity. Finally, we confirmed our findings in
99 spatially-explicit stochastic simulations of fitted time series from our mean field model. We
100 hypothesized that top-down immune processes would overrule classical resource-limitation in
101 bat cell lines described as constitutively antiviral in the literature, offering a testable prediction
102 for models fit to empirical data. We further predicted that the most robust antiviral responses
103 would be associated with the most rapid within-host virus propagation rates but also protect cells
104 against virus-induced mortality to support the longest enduring infections in tissue culture.
105

106 **Results**

107 **Virus infection experiments in antiviral bat cell cultures yield reduced cell mortality and**
108 **elongated epidemics.**

109 We first explored the influence of innate immune phenotype on within-host viral
110 propagation in a series of infection experiments in cell culture. We conducted plaque assays on
111 six-well plate monolayers of three immortalized mammalian kidney cell lines: [1] Vero (African
112 green monkey) cells, which are IFN-defective and thus limited in antiviral capacity (Desmyter,
113 Melnick, and Rawls 1968); [2] RoNi/7.1 (*Rousettus aegyptiacus*) cells which demonstrate
114 idiosyncratic induced interferon responses upon viral challenge (Kuzmin et al. 2017; Arnold et

115 al. 2018; Biesold et al. 2011; Pavlovich et al. 2018); and [3] PaKiT01 (*Pteropus alecto*) cells
116 which constitutively express IFN-α (Zhou et al. 2016; Crameri et al. 2009). To intensify cell
117 line-specific differences in constitutive immunity, we carried out infectivity assays with GFP-
118 tagged, replication-competent vesicular stomatitis Indiana viruses: rVSV-G, rVSV-EBOV, and
119 rVSV-MARV, which have been previously described (Miller et al. 2012; Wong et al. 2010).
120 Two of these viruses, rVSV-EBOV and rVSV-MARV, are recombinants for which cell entry is
121 mediated by the glycoprotein of the bat-evolved filoviruses, Ebola (EBOV) and Marburg
122 (MARV), thus allowing us to modulate the extent of structural, as well as immunological,
123 antiviral defense at play in each infection. Previous work in this lab has demonstrated
124 incompatibilities in the NPC1 filovirus receptor which render PaKiT01 cells refractory to
125 infection with rVSV-MARV (Ng and Chandran 2018), making them structurally antiviral, over
126 and above their constitutive expression of IFN-α. All three cell lines were challenged with all
127 three viruses at two multiplicities of infection (MOI): 0.001 and 0.0001. Between 18-39 trials
128 were run at each cell-virus-MOI combination, excepting rVSV-MARV infections on PaKiT01
129 cells at MOI=0.001, for which only 8 trials were run (see Materials and Methods; SI Appendix,
130 Figure S1-S3, Dataset S1).
131 Because plaque assays restrict viral transmission neighbor-to-neighbor in two-
132 dimensional cellular space (Howat et al. 2006), we were able to track the spread of GFP-
133 expressing virus-infected cells across tissue monolayers via inverted fluorescence microscopy.
134 For each infection trial, we monitored and re-imaged plates for up to 200 hours of observations
135 or until total monolayer destruction, processed resulting images, and generated a time series of
136 the proportion of infectious-cell occupied plate space across the duration of each trial (see
137 Materials and Methods). We used generalized additive models to infer the time course of all cell

138 culture replicates and construct the multi-trial dataset to which we eventually fit our mechanistic

139 transmission model for each cell line-virus-specific combination (Figure 1; SI Appendix, Figure

140 S2-S5).

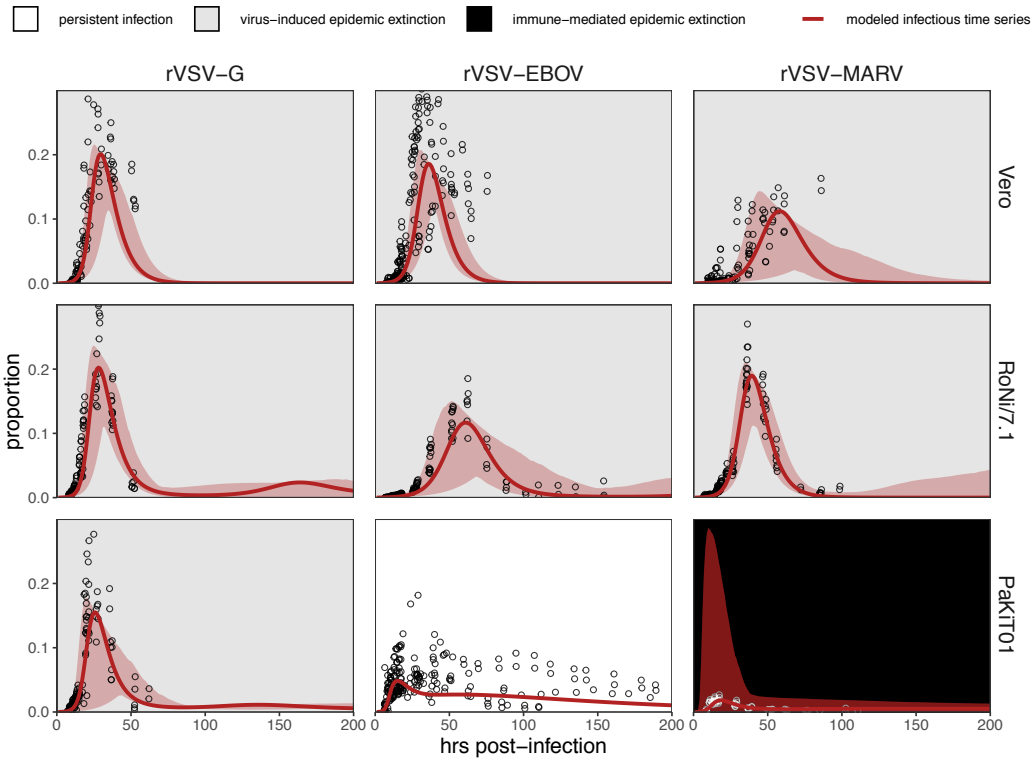

141

142 **Figure 1.** Fitted time series of infectious cell proportions from mean field model for rVSV-G,
143 rVSV-EBOV, and rVSV-MARV infections (columns) on Vero, RoNi/7.1, and PaKiT01 cell
144 lines (rows) at MOI=0.001. Results are shown for the best fit immune absent model on Vero
145 cells, induced immunity model on RoNi/7.1 cells, and constitutive (for rVSV-VSVG and rVSV-
146 EBOV) and induced (for rVSV-MARV) immunity models on PaKiT01 cells. Raw data across all
147 trials are shown as open circles (statistical smoothers from each trial used for fitting are available
148 in SI Appendix, Figure S2-S3). Model output is shown as a solid crimson line (95% confidence
149 intervals by standard error = red shading). Panel background corresponds to empirical outcome
150 of the average stochastic cell culture trial (persistent infection = white; virus-induced epidemic
151 extinction = gray; immune-mediated epidemic extinction = black). Parameter values are listed in
152 Table 1 and S1. Results for absent/induced/constitutive fitted models across all cell lines are
153 shown in SI Appendix, Figure S6 (MOI=0.001) and S7 (MOI=0.0001).
154

155 All three recombinant vesicular stomatitis viruses (rVSV-G, rVSV-EBOV, and rVSV-

156 MARV) infected Vero, RoNi/7.1, and PaKiT01 tissue cultures at both focal MOIs. Post-

157 invasion, virus spread rapidly across most cell monolayers, resulting in virus-induced epidemic
158 extinction. Epidemics were less severe in bat cell cultures, especially when infected with the
159 recombinant filoviruses, rVSV-EBOV and rVSV-MARV. Monolayer destruction was avoided in
160 the case of rVSV-EBOV and rVSV-MARV infections on PaKiT01 cells: in the former, persistent
161 viral infection was maintained throughout the 200-hour duration of each experiment, while, in
162 the latter, infection was eliminated early in the time series, preserving a large proportion of live,
163 uninfectious cells across the duration of the experiment. We assumed this pattern to be the result
164 of immune-mediated epidemic extinction (Figure 1). Patterns from MOI=0.001 were largely
165 recapitulated at MOI = 0.0001, though at somewhat reduced total proportions (SI Appendix,
166 Figure S5).
167
168 **A theoretical model fit to *in vitro* data recapitulates expected immune phenotypes for bat**
169 **cells.**
170 We next developed a within-host model to fit to these data in order to elucidate the
171 effects of induced and constitutive immunity on the dynamics of viral spread in host tissue
172 (Figure 1). The compartmental within-host system mimicked our two-dimensional cell culture
173 monolayer, with cells occupying five distinct infection states: susceptible (S), antiviral (A),
174 exposed (E), infectious (I), and dead (D). We modeled exposed cells as infected but not yet
175 infectious, capturing the 'eclipse phase' of viral integration into a host cell which precedes viral
176 replication. Antiviral cells were immune to viral infection, in accordance with the "antiviral
177 state" induced from interferon stimulation of ISGs in tissues adjacent to infection (Stetson and
178 Medzhitov 2006). Because we aimed to translate available data into modeled processes, we did
179 not explicitly model interferon dynamics but instead scaled the rate of cell progression from

180 susceptible to antiviral (ρ) by the proportion of exposed cells (globally) in the system. In systems
181 permitting constitutive immunity, a second rate of cellular acquisition of antiviral status (ε)
182 additionally scaled with the global proportion of susceptible cells in the model. Compared with
183 virus, IFN particles are small and highly diffusive, justifying this global signaling assumption at
184 the limited spatial extent of a six well plate and maintaining consistency with previous modeling
185 approximations of IFN signaling in plaque assay (Howat et al. 2006).

186 To best represent our empirical monolayer system, we expressed our state variables as
187 proportions (P_s, P_A, P_E, P_I, and P_D), under assumptions of frequency-dependent transmission in a
188 well-mixed population (Keeling and Rohani 2008), though note that the inclusion of P_D
189 (representing the proportion of dead space in the modeled tissue) had the functional effect of
190 varying transmission with infectious cell density. This resulted in the following system of
191 ordinary differential equations:

192

193 $$\frac{dP_s}{dt} = bP_D(P_s + P_A) - \beta P_S P_I - \mu P_s - \rho P_E P_s - \varepsilon P_s + cP_A \quad (1)$$

194 $$\frac{dP_A}{dt} = \rho P_E P_s + \varepsilon P_s - cP_A - \mu P_A \quad (2)$$

195 $$\frac{dP_E}{dt} = \beta P_S P_I - \sigma P_E - \mu P_E \quad (3)$$

196 $$\frac{dP_I}{dt} = \sigma P_E - \alpha P_I - \mu P_I \quad (4)$$

197 $$\frac{dP_D}{dt} = \mu(P_s + P_E + P_I + P_A) + \alpha P_I - bP_D(P_s + P_A) \quad (5)$$

198

199 We defined "induced immunity" as complete, modeling all cells as susceptible to viral
200 invasion at disease free equilibrium, with defenses induced subsequent to viral exposure through
201 the term ρ. By contrast, we allowed the extent of constitutive immunity to vary across the

202 parameter range of $\varepsilon > 0$, defining a "constitutive" system as one containing *any* antiviral cells at
203 disease free equilibrium. In fitting this model to tissue culture data, we independently estimated
204 both ρ and ε, as well as the cell-to-cell transmission rate, β, for each cell-virus combination.
205 Since the extent to which constitutively-expressed IFN-α is constitutively translated into
206 functional protein is not yet known for bat hosts (Zhou et al. 2016), this approach permitted our
207 tissue culture data to drive modeling inference: even in PaKiT01 cell lines known to
208 constitutively express IFN-α, the true constitutive extent of the system (i.e. the quantity of
209 antiviral cells present at disease free equilibrium) was allowed to vary through estimation of ε.
210 For the purposes of model-fitting, we fixed the value of c, the return rate of antiviral cells to
211 susceptible status, at 0. The small spatial scale and short time course (max 200 hours) of our
212 experiments likely prohibited any return of antiviral cells to susceptible status in our empirical
213 system; nonetheless, we retained the term c in analytical evaluations of our model because
214 regression from antiviral to susceptible status is possible over long time periods *in vitro* and at
215 the scale of a complete organism (Samuel and Knutson 1982; Rasmussen and Farley 1975;
216 Radke et al. 1974).

217 Before fitting to empirical time series, we undertook bifurcation analysis of our
218 theoretical model and generated testable hypotheses on the basis of model outcomes. From our
219 within-host model system (equations 1-5), we derived the following expression for R_0, the
220 pathogen basic reproduction number:

221 $$R_0 = \frac{\beta\sigma(b-\mu)(c+\mu)}{b(\sigma+\mu)(\alpha+\mu)(c+\mu+\varepsilon)} \quad (6)$$

222 Pathogens can invade a host tissue culture when $R_0 > 1$. Rapid rates of constitutive antiviral
223 acquisition (ε) will drive $R_0 < 1$: tissue cultures with highly constitutive antiviral immunity will
224 be therefore resistant to virus invasion from the outset. Since, by definition, induced immunity is

stimulated following initial virus invasion, the rate of induced antiviral acquisition (ρ) is not incorporated into the equation for R_0; while induced immune processes can control virus after initial invasion, they cannot prevent it from occurring to begin with. In cases of fully induced or absent immunity ($\varepsilon = 0$), the R_0 equation thus reduces to a form typical of the classic SEIR model:

$$R_0 = \frac{\beta\sigma(b-\mu)}{b(\alpha+\mu)(\sigma+\mu)} \quad (7)$$

At equilibrium, the theoretical, mean field model demonstrates one of three infection states: endemic equilibrium, stable limit cycles, or no infection (Figure 2). Respectively, these states approximate the persistent infection, virus-induced epidemic extinction, and immune-mediated epidemic extinction phenotypes previously witnessed in tissue culture experiments (Figure 1). Theoretically, endemic equilibrium is maintained when new infections are generated at the same rate at which infections are lost, while limit cycles represent parameter space under which infectious and susceptible populations are locked in predictable oscillations. Endemic equilibriums resulting from cellular regeneration (i.e. births) have been described *in vivo* for HIV (Coffin 1995) and *in vitro* for herpesvirus plaque assays (Howat et al. 2006), but, because they so closely approach zero, true limit cycles likely only occur theoretically, instead yielding stochastic extinctions in empirical time series.

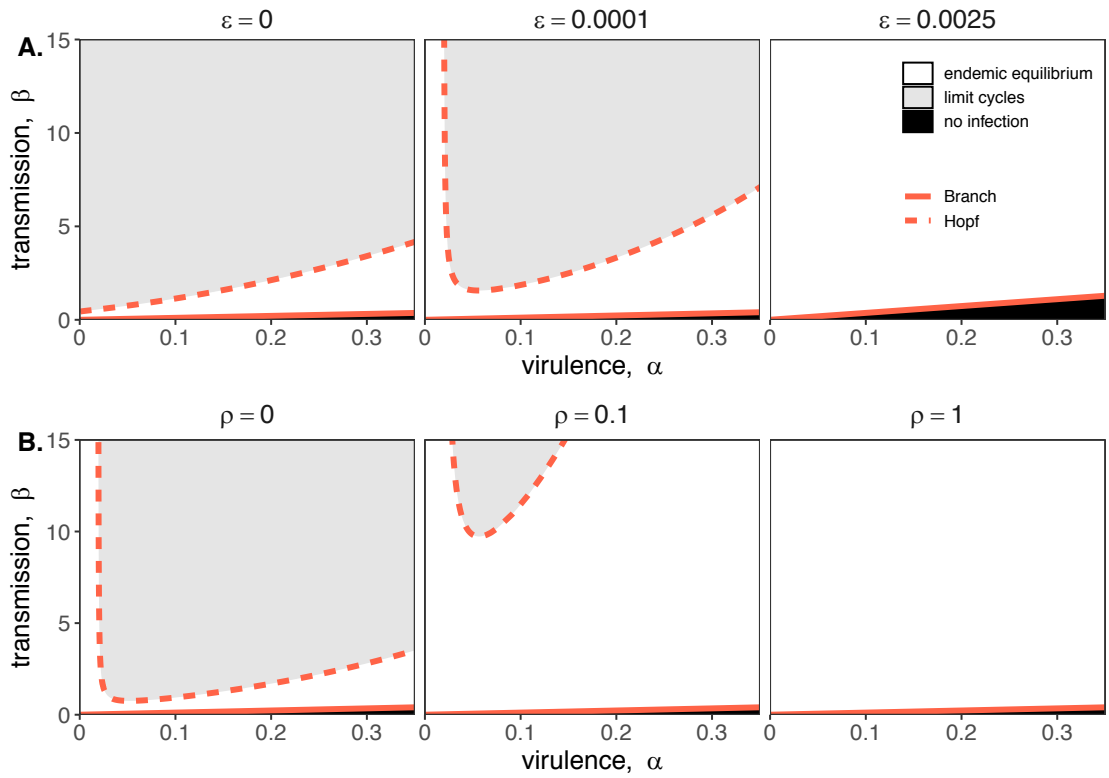

Figure 2. Two parameter bifurcations of the mean field model, showing variation in the transmission rate, β, against variation in the pathogen-induced mortality rate, α, under diverse immune assumptions. Panel (A) depicts dynamics under variably constitutive immunity, ranging from absent (left: $\varepsilon = 0$) to high (right: $\varepsilon = .0025$). In all panel (A) plots, the rate of induced immune antiviral acquisition (ρ) was fixed at 0.01. Panel (B) depicts dynamics under variably induced immunity, ranging from absent (left: ρ=0) to high (right: ρ=1). In all panel (B) plots, the rate of constitutive antiviral acquisition (ε) was fixed at 0.0001. Branch point curves are represented as solid lines and Hopf curves as dashed lines. White space indicates endemic equilibrium (persistence), gray space indicates limit cycles, and black space indicates no infection (extinction). Other parameter values for equilibrium analysis were fixed at: b = .025, μ = .001, σ = 1/6, c = 0. Special points from bifurcations analyses are listed in SI Appendix, Table S2.

Bifurcation analysis of our mean field model revealed that regions of no infection (pathogen extinction) were bounded at lower threshold (Branch point) values for β, below which the pathogen was unable to invade. We found no upper threshold to invasion for β under any circumstances (i.e. β high enough to drive pathogen-induced extinction), but high β values resulted in Hopf bifurcations, which delineate regions of parameter space characterized by limit

cycles. Since limit cycles so closely approach zero, high βs recovered in this range would likely produce virus-induced epidemic extinctions under experimental conditions. Under more robust representations of immunity, with higher values for either or both induced (ρ) and constitutive (ε) rates of antiviral acquisition, Hopf bifurcations occurred at increasingly higher values for β, meaning that persistent infections could establish at higher viral replication rates (Figure 2). Consistent with our derivation for R_0, we found that the Branch point threshold for viral invasion was independent of changes to the induced immune parameter (ρ) but saturated at high values of ε that characterize highly constitutive immunity (Figure 3).

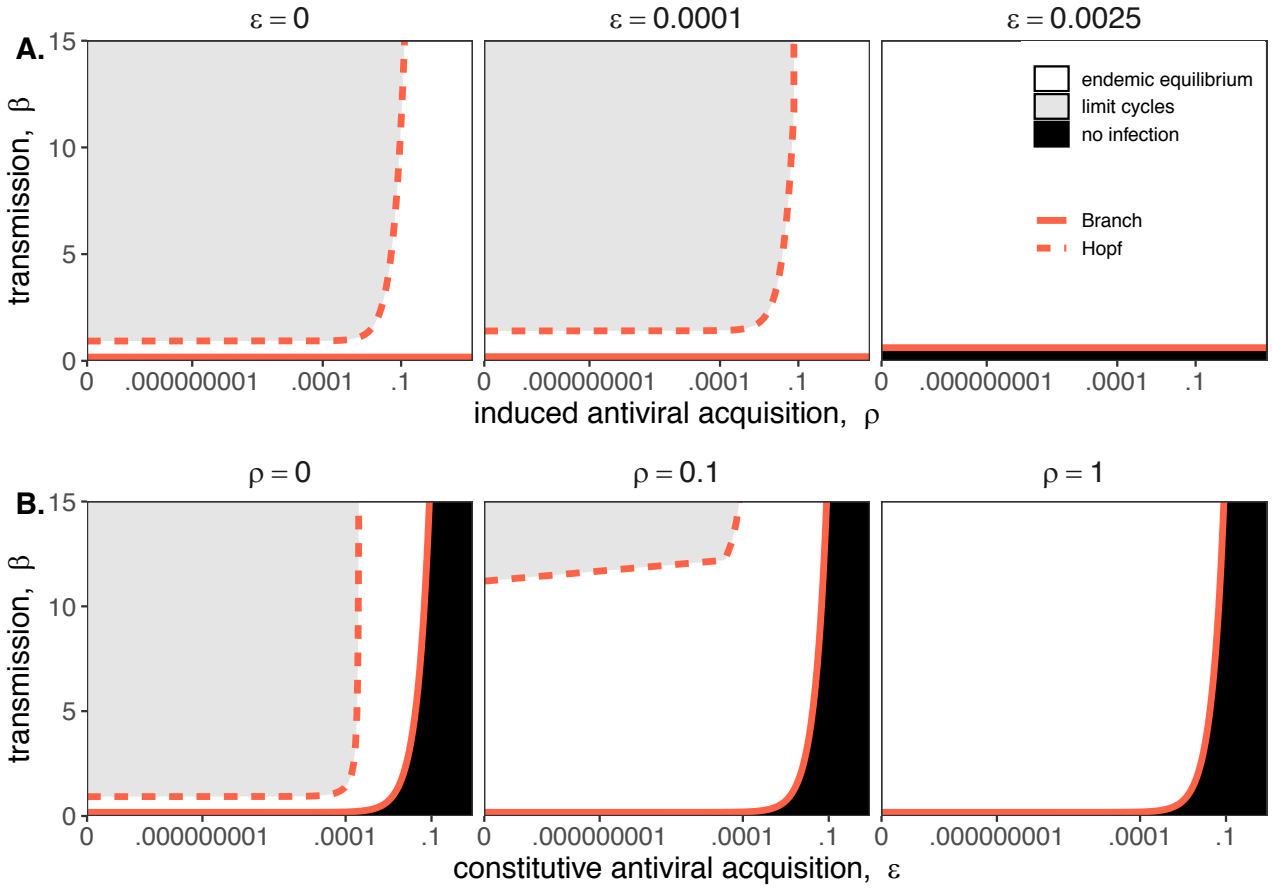

Figure 3. Two parameter bifurcations of the mean field model, showing variation in the transmission rate, β, against variation in: (A) the induced immunity rate of antiviral acquisition

(ρ) and (B) the constitutive immunity rate of antiviral acquisition (ε). Panels show variation in the extent of immunity, from absent (left) to high (right). Branch point curves are represented as solid lines and Hopf curves as dashed lines. White space indicates endemic equilibrium (persistence), gray space indicates limit cycling, and black space indicates no infection (extinction). Other parameter values for equilibrium analysis were fixed at: b = .025, μ = .001, σ = 1/6, α = 1/6, c = 0. Special points from bifurcations analyses are listed in SI Appendix, Table S2.

We next fit our theoretical model by least squares to each cell line-virus combination, under absent, induced, and constitutive assumptions of immunity. In general, best fit models recapitulated expected outcomes based on the immune phenotype of the cell line in question, as described in the general literature (Table 1; SI Appendix, Table S1). The absent immune model offered the most accurate approximation of IFN-deficient Vero cell time series, the induced immune model best recovered the RoNi/7.1 cell trials, and, in most cases, the constitutive immune model most closely recaptured infection dynamics across constitutively IFN-α-expressing PaKiT01 cell lines (Figure 1; SI Appendix, Figure S4-S5, Table S1). Ironically, the induced immune model offered a slightly better fit than the constitutive to rVSV-MARV infections on the PaKiT01 cell line (the one cell line-virus combination for which we know a constitutively antiviral cell-receptor incompatibility to be at play). Because constitutive immune assumptions can prohibit pathogen invasion ($R_0 < 1$), model fits to this time series under constitutive assumptions were handicapped by overestimations of ε, which prohibited pathogen invasion. Only by incorporating an exceedingly rapid rate of induced antiviral acquisition could the model guarantee that initial infection would be permitted and then rapidly controlled.

301 **Table 1. Optimized parameters from best fit deterministic model and spatial approximation**

Cell Line	Virus	Immune Assumption	Antiviral Rate	ε [lci – uci] *	ρ [lci – uci] *	β [lci – uci] *	mean field R_0	spatial β
Vero	rVSV-G	Absent	0	0 [0-0]	0 [0-0]	2.44 [1.52-3.36]	8.729	24.418
	rVSV-EBOV	Absent	0	0 [0-0]	0 [0-0]	1.5 [1.06-1.94]	5.416	14.996
	rVSV-MARV	Absent	0	0 [0-0]	0 [0-0]	0.975 [0.558-1.39]	3.454	9.752
RoNi/7.1	rVSV-G	Induced	7.03×10^{-5}	0 [0-0]	0.089 [0-0.432]	2.47 [1.49-3.45]	10.907	24.705
	rVSV-EBOV	Induced	2.87×10^{-5}	0 [0-0]	0.0363 [0-0.343]	0.685 [0.451-0.919]	3.043	6.849
	rVSV-MARV	Induced	1.40×10^{-5}	0 [0-0]	0.0177 [0-0.257]	1.23 [0.917-1.55]	5.475	12.324
PaKiT01	rVSV-G	Constitutive	.00209	0.00602 [0-0.019]	8.26×10^{-8} [0-4.75×10^{-7}]	3.45 [1.07-5.84]	6.189	34.516
	rVSV-EBOV	Constitutive	.00499	0.0478 [0-0.0958]	4.46×10^{-8} [0-4.37×10^{-7}]	34.5 [28.7-40.2]	18.823	344.821
	rVSV-MARV	Induced	.00687	0 [0-0]	13.1 [0-37.9]	3.25 [0-41.3]	8.828	32.452

302 * lci = lower and uci = upper 95% confidence interval. No confidence interval is shown for spatial β which was fixed at 10 times the estimated
303 mean for the mean field model fits when paired with equivalent values of ε and ρ.
304 All other parameters were fixed at the following values: b=.025; α = 1/6; c=0; μ= 1/121 (Vero), 1/191 (RoNi/7.1), and 1/84 (PaKiT01)
305

306 **Robust immunity is linked to rapid within-host virus transmission rates in fitted models.**

307 In fitting our theoretical model to *in vitro* data, we estimated the within-host virus
308 transmission rate (β) and the rate(s) of cellular acquisition to antiviral status (ρ or ρ + ε) (Table
309 1; SI Appendix, Table S1). Under absent immune assumptions, ρ and ε were fixed at 0 while β
310 was estimated; under induced immune assumptions, ε was fixed at 0 while ρ and β were
311 estimated; and under constitutive immune assumptions, all three parameters (ρ, ε, and β) were
312 simultaneously estimated for each cell-virus combination. Best fit parameter estimates for
313 MOI=0.001 data are visualized in conjunction with β – ρ and β – ε bifurcations in Figure 4; all
314 general patterns were recapitulated at lower values for β on MOI=0.0001 trials (SI Appendix,
315 Figure S6).

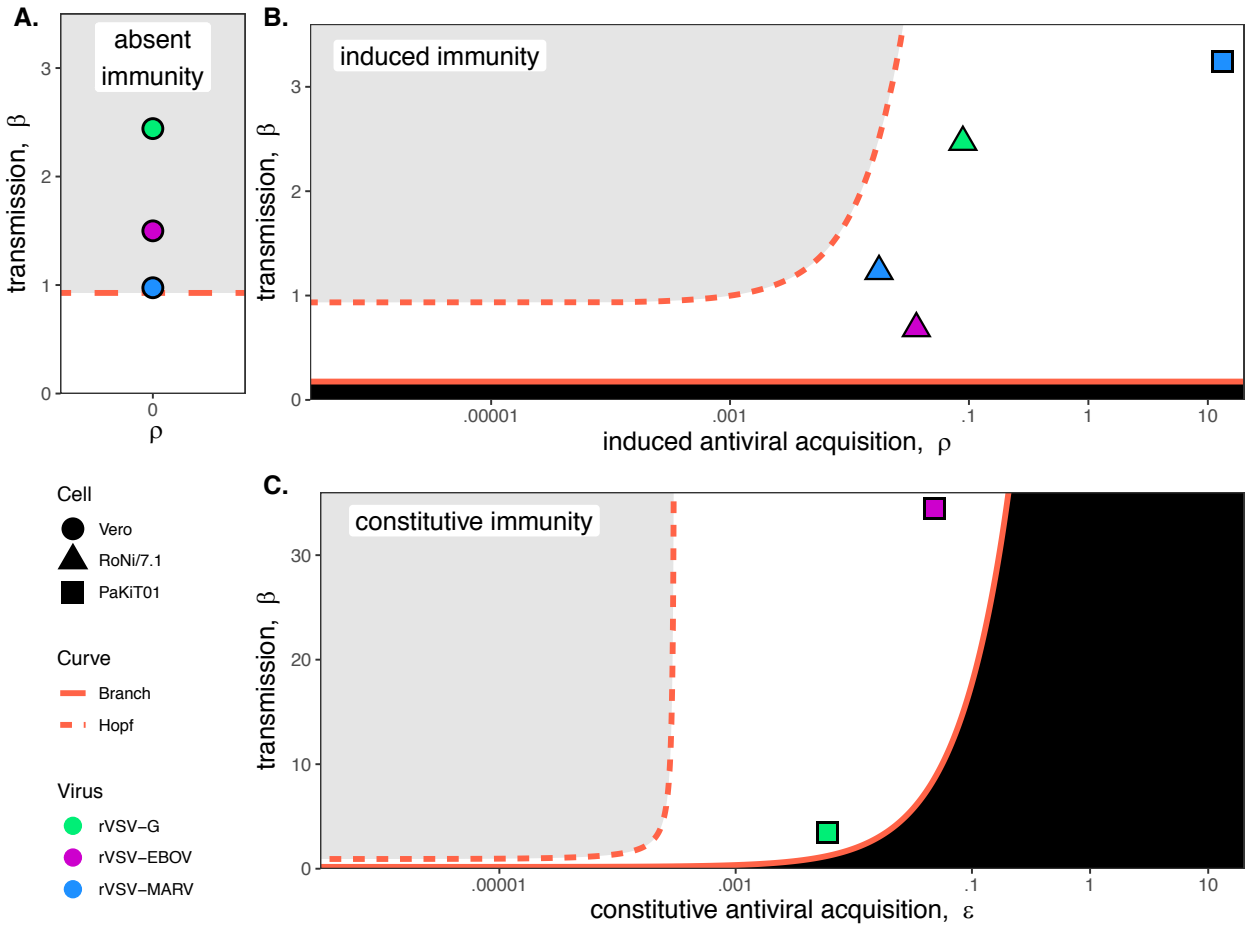

Figure 4. Best fit parameter estimates for β and ρ or *ε* from mean-field model fits to MOI=0.001 time series data, atop (A,B) β – ρ and (C) β – *ε* bifurcation. Fits and bifurcations are grouped by immune phenotype: (A) absent; (B) induced; (C) constitutive immunity, with cell lines differentiated by shape (Vero=circles; RoNi/7.1 = triangles; PaKiT01=squares) and viral infections by color (rVSV-G = green, rVSV-EBOV = magenta, rVSV-MARV = blue). Note that y-axis values are ten-fold higher in panel (C). Branch point curves (solid lines) and Hopf curves (dashed lines) are reproduced from Figure 3. White space indicates endemic equilibrium (pathogen persistence), gray space indicates limit cycling (virus-induced epidemic extinction), and black space indicates no infection (immune-mediated pathogen extinction). In panel (A) and (B), *ε* is fixed at 0; in panel (C), ρ is fixed at $5x10^{-8}$ for bifurcation curves and estimated at $4x10^{-8}$ and $8x10^{-8}$ for rVSV-EBOV and rVSV-G parameter points, respectively. Other parameter values were fixed at: $b = .025$, $\mu = 0.001$, $\sigma = 1/6$, $\alpha = 1/6$, and $c = 0$ across all panels. Raw fitted values and corresponding 95% confidence intervals for β, ρ, and *ε*, background parameter values, and AIC recovered from model fit, are reported in SI, Appendix Table S1. Parameter fits at MOI=0.0001 are visualized in SI Appendix, Figure S6.

As anticipated, the immune absent model (a simple target cell model) offered the best fit to IFN-deficient Vero cell infections (Figure 4, Table 1; SI Appendix, Figure S4-S5, Table S1).

336 Among Vero cell trials, infections with rVSV-G produced the highest β estimates, followed by
337 infections with rVSV-EBOV and rVSV-MARV. Best fit parameter estimates on Vero cell lines
338 localized in the region of parameter space corresponding to theoretical limit cycles, consistent
339 with observed virus-induced epidemic extinctions in stochastic tissue cultures.

340 In contrast to Vero cells, the induced immunity model offered the best fit to all RoNi/7.1
341 data, consistent with reported patterns in the literature and our own validation by qPCR (Table 1;
342 SI Appendix, Figure S7; Biesold et al. 2011; Kuzmin et al. 2017; Arnold et al. 2018; Pavlovich
343 et al. 2018). As in Vero cell trials, we estimated highest β values for rVSV-G infections on
344 RoNi/7.1 cell lines but here recovered higher β estimates for rVSV-MARV than for rVSV-
345 EBOV. This reversal was balanced by a higher estimated rate of acquisition to antiviral status (ρ)
346 for rVSV-EBOV versus rVSV-MARV. In general, we observed that more rapid rates of antiviral
347 acquisition (either induced, ρ, constitutive, ε, or both) correlated with higher transmission rates
348 (β). When offset by ρ, β values estimated for RoNi/7.1 infections maintained the same amplitude
349 as those estimated for immune-absent Vero cell lines but caused gentler epidemics and reduced
350 cellular mortality (Figure 1). RoNi/7.1 parameter estimates localized in the region corresponding
351 to endemic equilibrium for the deterministic, theoretical model (Figure 4), yielding less acute
352 epidemics which nonetheless went extinct in stochastic experiments.

353 Finally, rVSV-G and rVSV-EBOV trials on PaKiT01 cells were best fit by models
354 assuming constitutive immunity, while rVSV-MARV infections on PaKiT01 were matched
355 equivalently by models assuming either induced or constitutive immunity—with induced models
356 favored over constitutive in AIC comparisons because one fewer parameter was estimated (SI
357 Appendix, Figure S4-S5, Table S1). For all virus infections, PaKiT01 cell lines yielded β
358 estimates a full order of magnitude higher than Vero or RoNi/7.1 cells, with each β balanced by

359 an immune response (either ρ, or ρ combined with ε) also an order of magnitude higher than that
360 recovered for the other cell lines (Figure 4; Table 1). As in RoNi/7.1 cells, PaKiT01 parameter
361 fits localized in the region corresponding to endemic equilibrium for the deterministic theoretical
362 model. Because constitutive immune processes can actually prohibit initial pathogen invasion,
363 constitutive immune fits to rVSV-MARV infections on PaKiT01 cell lines consistently localized
364 at or below the Branch point threshold for virus invasion ($R_0 = 1$). During model fitting for
365 optimization of ε, any parameter tests of ε values producing $R_0 < 1$ resulted in no infection and,
366 consequently, produced an exceedingly poor fit to infectious time series data. In all model fits
367 assuming constitutive immunity, across all cell lines, parameter estimates for ρ and ε traded off,
368 with one parameter optimized at values approximating zero, such that the immune response was
369 modeled as almost entirely induced or entirely constitutive (Table 1; SI Appendix, Table S1). For
370 RoNi/7.1 cells, even when constitutive immunity was allowed, the immune response was
371 estimated as almost entirely induced, while for rVSV-G and rVSV-EBOV fits on PaKiT01 cells,
372 the immune response optimized as almost entirely constitutive. For rVSV-MARV on PaKiT01
373 cells, however, estimation of ρ was high under all assumptions, such that any additional antiviral
374 contributions from ε prohibited virus from invading at all. The induced immune model thus
375 produced a more parsimonious recapitulation of these data because virus invasion was always
376 permitted, then rapidly controlled.
377
378 **Antiviral cells safeguard live cells against rapid cell mortality to elongate epidemic**
379 **duration *in vitro.***
380 In order to compare the relative contributions of each cell line's disparate immune
381 processes to epidemic dynamics, we next used our mean field parameter estimates to calculate

382 the initial 'antiviral rate'—the initial accumulation rate of antiviral cells upon virus invasion for
383 each cell-virus-MOI combination—based on the following equation:
384
385 $$Antiviral\ Rate = \rho P_E P_S - \varepsilon P_S \quad (8)$$
386
387 where P_E was calculated from the initial infectious dose (MOI) of each infection experiment and
388 P_S was estimated at disease free equilibrium:
389
390 $$P_E = 1 - e^{-MOI} \quad (9)$$
391 $$P_S = \frac{(b-\mu)(c+\mu)}{b(c+\mu+\varepsilon)} \quad (10)$$
392
393 Because ρ and ε both contribute to this initial antiviral rate, induced and constitutive immune
394 assumptions are capable of yielding equally rapid rates, depending on parameter fits. Indeed,
395 under fully induced immune assumptions, the induced antiviral acquisition rate (ρ) estimated for
396 rVSV-MARV infection on PaKiT01 cells was so high that the initial antiviral rate exceeded even
397 that estimated under constitutive assumptions for this cell-virus combination (SI Appendix,
398 Table S1). In reality, we know that NPC1 receptor incompatibilities make PaKiT01 cell lines
399 constitutively refractory to rVSV-MARV infection (Ng and Chandran 2018) and that PaKiT01
400 cells also constitutively express the antiviral cytokine, IFN-α. Model fitting results suggest that
401 this constitutive expression of IFN-α may act more as a rapidly inducible immune response
402 following virus invasion than as a constitutive secretion of functional IFN-α protein.
403 Nonetheless, as hypothesized, PaKiT01 cell lines were by far the most antiviral of any in our
404 study—with initial antiviral rates estimated several orders of magnitude higher than any others in

405 our study, under either induced or constitutive assumptions (Table 1; SI Appendix, Table S1).
406 RoNi/7.1 cells displayed the second-most-pronounced signature of immunity, followed by Vero
407 cells, for which the initial antiviral rate was essentially zero even under forced assumptions of
408 induced or constitutive immunity (Table 1; SI Appendix, Table S1).

409 Using fitted parameters for β and ε, we additionally calculated R_0, the basic reproduction
410 number for the virus, for each cell line-virus-MOI combination (Table 1; SI Appendix, Table
411 S1). We found that R_0 was essentially unchanged across differing immune assumptions for
412 RoNi/7.1 and Vero cells, for which the initial antiviral rate was low. In the case of PaKiT01
413 cells, a high initial antiviral rate under either induced or constitutive immunity resulted in a
414 correspondingly high estimation of β (and, consequently, R_0) which still produced the same
415 epidemic curve that resulted from the much lower estimates for β and R_0 paired with absent
416 immunity. These findings suggest that antiviral immune responses protect host tissues against
417 virus-induced cell mortality to permit the establishment of more rapid within-host transmission
418 rates.

419 Total monolayer destruction occurred in all cell-virus combinations excepting rVSV-
420 EBOV infections on RoNi/7.1 cells and rVSV-EBOV and rVSV-MARV infections on PaKiT01
421 cells. Monolayer destruction corresponded to susceptible cell depletion and epidemic turnover
422 where R-effective (the product of R_0 and the proportion susceptible) was reduced below one
423 (Figure 5). For rVSV-EBOV infections on RoNi/7.1, induced antiviral cells safeguarded remnant
424 live cells, which birthed new susceptible cells late in the time series. In rVSV-EBOV and rVSV-
425 MARV infections on PaKiT01 cells, this antiviral protection halted the epidemic (Figure 5; R-
426 effective <1) before susceptibles fully declined. In the case of rVSV-EBOV on PaKiT01, the
427 birth of new susceptibles from remnant live cells protected by antiviral status maintained late-

stage transmission to facilitate long-term epidemic persistence. Importantly, under fixed parameter values for the infection incubation rate (σ) and infection-induced mortality rate (α), models were unable to reproduce the longer-term infectious time series captured in data from rVSV-EBOV infections on PaKiT01 cell lines without incorporation of cell births, an assumption adopted in previous modeling representations of IFN-mediated viral dynamics in tissue culture (Howat et al. 2006). In our experiments, we observed that cellular reproduction took place as plaque assays achieved confluency.

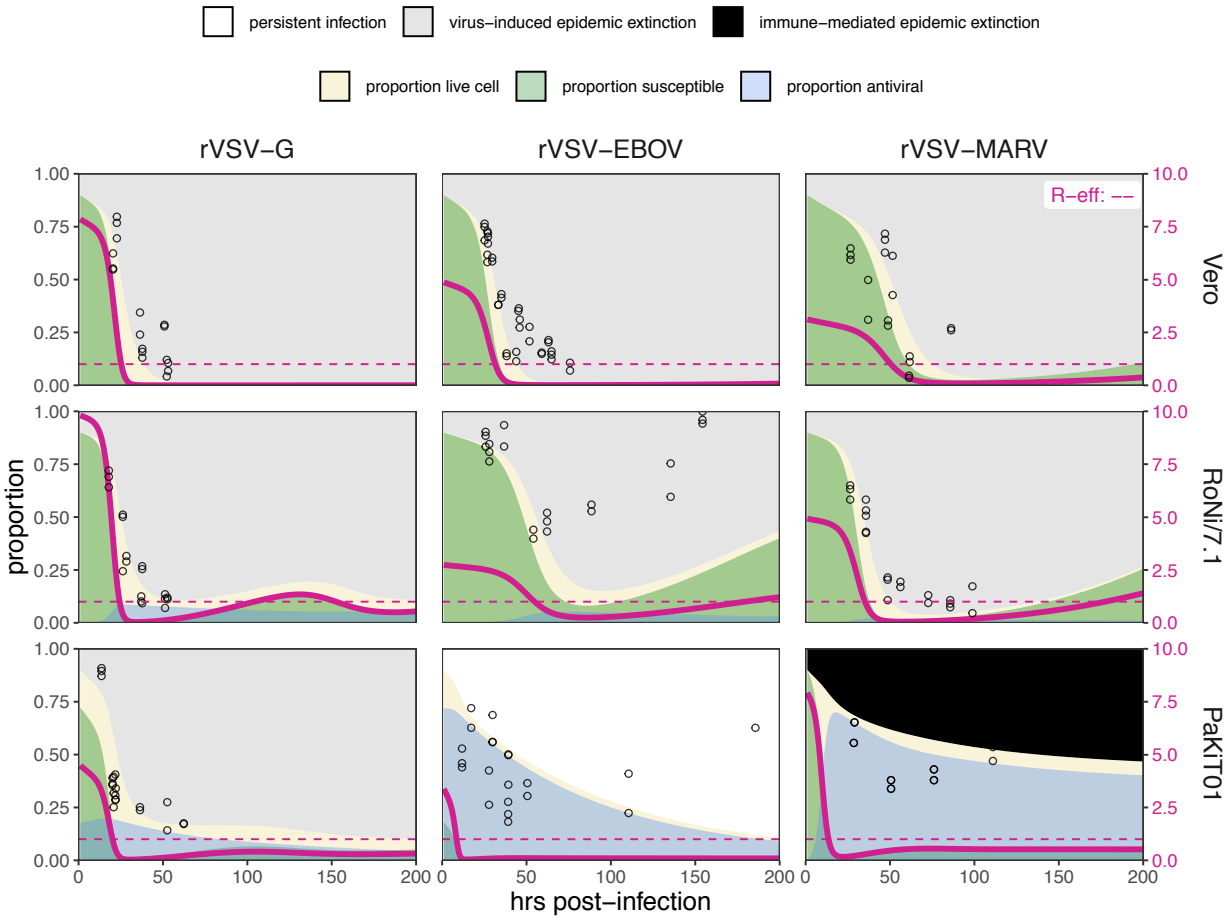

Figure 5. Fitted time series of susceptible (green shading) and antiviral (blue shading) cell proportions from the mean field model for rVSV-G, rVSV-EBOV, and rVSV-MARV infections

(columns) on Vero, RoNi/7.1, and PaKiT01 cell lines (rows) at MOI=0.001. Results are shown for the best fit immune absent model on Vero cells, induced immunity model on RoNi/7.1 cells and constitutive (rVSV-G and rVSV-EBOV) and induced (rVSV-MARV) immune models on PaKiT01 cells. Combined live, uninfectious cell populations (S + A + E) are shown in tan shading, with raw live, uninfectious cell data from Hoechst stains visualized as open circles. The right-hand y-axis corresponds to R-effective (pink solid line) across each time series; R-effective =1 is a pink dashed, horizontal line. Panel background corresponds to empirical outcome of the average stochastic cell culture trial (persistent infection = white; virus-induced epidemic extinction = gray; immune-mediated epidemic extinction = black). Parameter values are listed in SI Appendix, Table S1 and results for absent/induced/constitutive fitted models across all cell lines in Figure S8 (MOI=0.001) and S9 (MOI=0.0001).

Finally, because the protective effect of antiviral cells is more clearly observable spatially, we confirmed our results by simulating fitted time series in a spatially-explicit, stochastic reconsttruction of our mean field model. In spatial simulations, rates of antiviral acquisition were fixed at fitted values for ρ and ε derived from mean field estimates, while transmission rates (β) were fixed at values ten times greater than those estimated under mean field conditions because spatial structure is known to intensify parameter thresholds permitting pathogen invasion (Webb, Keeling and Boots, 2007; SI Appendix, Figure S10, Video S1-S3). In immune capable time series, spatial antiviral cells acted as 'refugia' which protected live cells from infection as each initial epidemic wave 'washed' across a cell monolayer. Eventual birth of new susceptibles from these living refugia allowed for sustained epidemic transmission in cases where some infectious cells persisted at later timepoints in simulation (SI Appendix, Figure S10, Video S1-S3).

Discussion

Bats are reservoirs for several important emerging zoonoses but appear not to experience disease from otherwise virulent viral pathogens. Though the molecular biological literature has made great progress in elucidating the mechanisms by which bats tolerate viral infections (Zhou

469 et al. 2016; Ahn et al. 2019; Xie et al. 2018; Pavlovich et al. 2018; Zhang et al. 2013), the impact
470 of unique bat immunity on virus dynamics within-host has not been well-elucidated. We used an
471 innovative combination of *in vitro* experimentation and within-host modeling to explore the
472 impact of unique bat immunity on virus dynamics. Critically, we found that bat cell lines
473 demonstrated a signature of enhanced interferon-mediated immune response, of either
474 constitutive or induced form, which allowed for establishment of rapid within-host, cell-to-cell
475 virus transmission rates (β). These results were supported by both data-independent bifurcation
476 analysis of our mean field theoretical model, as well as fitting of this model to viral infection
477 time series established in bat cell culture. Additionally, we demonstrated that the antiviral state
478 induced by the interferon pathway protects live cells from mortality in tissue culture, resulting in
479 *in vitro* epidemics of extended duration that enhance that probability of establishing a long-term
480 persistent infection. Our findings suggest that viruses evolved in bat reservoirs possessing
481 enhanced IFN capabilities could achieve more rapid within-host transmission rates without
482 causing pathology to their hosts. Such rapidly-reproducing viruses would likely generate extreme
483 virulence upon spillover to hosts lacking similar immune capacities to bats.

484 To achieve these results, we first developed a novel, within-host, theoretical model
485 elucidating the effects of unique bat immunity, then undertook bifurcation analysis of the
486 model's equilibrium properties under immune absent, induced, and constitutive assumptions. We
487 considered a cell line to be constitutively immune if possessing any number of antiviral cells at
488 disease free equilibrium but allowed the extent of constitutive immunity to vary across the
489 parameter range for ε, the constitutive rate of antiviral acquisition. In deriving the equation for
490 R_0, the basic reproduction number, which defines threshold conditions for virus invasion of a
491 tissue ($R_0 > 1$), we demonstrated how the invasion threshold is elevated at high values of

492 constitutive antiviral acquisition, ε. Constitutive immune processes can thus prohibit pathogen
493 invasion, while induced responses, by definition, can only control infections *post-hoc*. Once
494 thresholds for pathogen invasion have been met, assumptions of constitutive immunity will limit
495 the cellular mortality (virulence) incurred at high transmission rates. Regardless of mechanism
496 (induced or constitutive), interferon-stimulated antiviral cells appear to play a key role in
497 maintaining longer term or persistent infections by safeguarding susceptible cells from rapid
498 infection and concomitant cell death.

499 Fitting of our model to *in vitro* data supported expected immune phenotypes for different
500 bat cell lines as described in the literature. Simple target cell models that ignore the effects of
501 immunity best recapitulated infectious time series derived from IFN-deficient Vero cells, while
502 models assuming induced immune processes most accurately reproduced trials derived from
503 RoNi/7.1 (*Rousettus aegyptiacus*) cells, which possesses a standard virus-induced IFN-response.
504 In most cases, models assuming constitutive immune processes best recreated virus epidemics
505 produced on PaKiT01 (*Pteropus alecto*) cells, which are known to constitutively express the
506 antiviral cytokine, IFN-α (Zhou et al. 2016). Model support for induced immune assumptions in
507 fits to rVSV-MARV infections on PaKiT01cells suggests that the constitutive IFN-α expression
508 characteristic of *P. alecto* cells may represent more of a constitutive immune priming process
509 than a perpetual, functional, antiviral defense. Results from mean field model fitting were
510 additionally confirmed in spatially explicit stochastic simulations of each time series.

511 As previously demonstrated in within-host models for HIV (Coffin 1995; Perelson et al.
512 1996; Nowak et al. 1995; Bonhoeffer et al. 1997; Ho et al. 1995), assumptions of simple target-
513 cell depletion can often provide satisfactory approximations of viral dynamics, especially those
514 reproduced in simple *in vitro* systems. Critically, our model fitting emphasizes the need for

515 incorporation of top-down effects of immune control in order to accurately reproduce infectious
516 time series derived from bat cell tissue cultures, especially those resulting from the robustly
517 antiviral PaKiT01 *P. alecto* cell line. These findings indicate that enhanced IFN-mediated
518 immune pathways in bat reservoirs may promote elevated within-host virus replication rates
519 prior to cross-species emergence. We nonetheless acknowledge the limitations imposed by *in*
520 *vitro* experiments in tissue culture, especially involving recombinant viruses and immortalized
521 cell lines. Future work should extend these cell culture studies to include measurements of
522 multiple state variables (i.e. antiviral cells) to enhance epidemiological inference.
523 The continued recurrence of Ebola epidemics across central Africa highlights the
524 importance of understanding bats' roles as reservoirs for virulent zoonotic disease. The past
525 decade has born witness to emerging consensus regarding the unique pathways by which bats
526 resist and tolerate highly virulent infections (Brook and Dobson 2015; Xie et al. 2018; Zhang et
527 al. 2013; Ahn et al. 2019; Zhou et al. 2016; Ng et al. 2015; Pavlovich et al. 2018). Nonetheless,
528 an understanding of the mechanisms by which bats support endemic pathogens at the population
529 level, or promote the evolution of virulent pathogens at the individual level, remains elusive.
530 Endemic maintenance of infection is a defining characteristic of a pathogen reservoir (Haydon et
531 al. 2002), and bats appear to merit such a title, supporting long-term persistence of highly
532 transmissible viral infections in isolated island populations well below expected critical
533 community sizes (Peel et al. 2012). Researchers debate the relative influence of population-level
534 and within-host mechanisms which might explain these trends (Plowright et al. 2016), but
535 increasingly, field data are difficult to reconcile without acknowledgement of a role for persistent
536 infections (Peel et al. 2018; Brook et al. 2019). We present general methods to study cross-scale
537 viral dynamics, which suggest that within-host persistence is supported by robust antiviral

538 responses characteristic of bat immune processes. Viruses which evolve rapid replication rates
539 under these robust antiviral defenses may pose the greatest hazard for cross-species pathogen
540 emergence into spillover hosts with immune systems that differ from those unique to bats.
541
542
543
544
545
546
547
548
549
550
551
552
553
554
555
556
557
558
559
560

561 **Materials and Methods**

562

Key Resources Table*				
Reagent type (species) or resource	**Designation**	**Source or reference**	**Identifiers**	**Additional information**
cell line (Vero)	Kidney (normal, epithelial, adult)	ATCC	CCL-81	
cell line (*Rousettus aegyptiacus)*	Kidney (normal, epithelial, adult)	(Biesold et al. 2011; Kühl et al. 2011)	RoNi/7.1	
cell line (*Pteropus alecto*)	Kidney (normal, epithelial, adult)	(Crameri et al. 2009)	PaKiT01	
virus strain	Replication competent, recombinant vesicular stomatitis Indiana virus expressing eGFP	(Miller et al. 2012; Wong et al. 2010)	rVSV-G	
virus strain	Replication competent, recombinant vesicular stomatitis Indiana virus expressing eGFP & EBOV GP in place of VSV G	(Miller et al. 2012; Wong et al. 2010)	rVSV-EBOV	
virus strain	Replication competent, recombinant vesicular stomatitis Indiana virus expressing eGFP & MARV GP in place of VSV G	(Miller et al. 2012; Wong et al. 2010)	rVSV-MARV	
reagent	Hoechst 33342 Fluorescent Stain	ThermoFisher	cat #: 62249	
reagent	L-Glutamine Solution	ThermoFisher	cat #: 25030081	
reagent	Gibco HEPES	ThermoFisher	cat #: 15630080	

reagent	iTaq Universal SYBR Green Supermix	BioRad	cat #: 1725120	
commercial assay or kit	Quick RNA Mini Prep Kit	Zymo	cat #: R1054	
commercial assay or kit	Invitrogen Superscript III cDNA Synthesis Kit	ThermoFisher	cat #: 18080051	
software	MatCont (version 2.2)	(Dhooge et al. 2008)	MatCont	
R	R version 3.6.0	(R Core Team 2019)	R	
*Note that primers for *R. aegyptiacus* and *P. alecto* β-Actin, IFN-α, and IFN-β genes are listed in the SI Appendix, Table S3.				

563

564 **Cell Culture Experiments.**

565 *Cells.*

566 All experiments were carried out on three immortalized mammalian kidney cell lines:
567 Vero (African green monkey), RoNi/7.1 (*Rousettus aegyptiacus*) (Kühl et al. 2011; Biesold et al.
568 2011) and PaKiT01 (*Pteropus alecto*) (Crameri et al. 2009). The species identification of all bat
569 cell lines were confirmed morphologically and genetically in the publications in which they were
570 originally described (Kühl et al. 2011; Biesold et al. 2011; Crameri et al. 2009). Vero cells were
571 obtained from ATCC.

572 Monolayers of each cell line were grown to 90% confluency (~9 x 10^5 cells) in 6-well
573 plates. Cells were maintained in a humidified 37˚C, 5% CO_2 incubator and cultured in
574 Dulbecco's modified Eagle medium (DMEM) (Life Technologies, Grand Island, NY),
575 supplemented with 2% fetal bovine serum (FBS) (Gemini Bio Products, West Sacramento, CA),
576 and 1% penicillin-streptomycin (Life Technologies). Cells were tested monthly for mycoplasma

577 contamination while experiments were taking place; all cells assayed negative for contamination
578 at every testing.
579 Previous work has demonstrated that all cell lines used are capable of mounting a type I
580 IFN response upon viral challenge, with the exception of Vero cells, which possess an IFN-β
581 deficiency (Desmyter, Melnick, and Rawls 1968; Rhim et al. 1969; Emeny and Morgan 1979).
582 RoNi/7.1 cells have been shown to mount idiosyncratic induced IFN defenses upon viral
583 infection (Pavlovich et al. 2018; Kuzmin et al. 2017; Arnold et al. 2018; Kühl et al. 2011;
584 Biesold et al. 2011), while PaKiT01 cells are known to constitutively express the antiviral
585 cytokine, IFN-α (Zhou et al. 2016). This work is the first documentation of IFN signaling
586 induced upon challenge with the particular recombinant VSVs outlined below. We verified
587 known antiviral immune phenotypes via qPCR. Results were consistent with the literature,
588 indicating a less pronounced role for interferon defense against viral infection in RoNi/7.1 versus
589 PaKiT01 cells.
590
591 *Viruses.*
592 Replication-capable recombinant vesicular stomatitis Indiana viruses, expressing filovirus
593 glycoproteins in place of wild type G (rVSV-G, rVSV-EBOV, and rVSV-MARV) have been
594 previously described (Wong et al. 2010; Miller et al. 2012). Viruses were selected to represent a
595 broad range of anticipated antiviral responses from host cells, based on a range of past
596 evolutionary histories between the virus glycoprotein mediating cell entry and the host cell's
597 entry receptor. These interactions ranged from the total absence of evolutionary history in the
598 case of rVSV-G infections on all cell lines to a known receptor-level cell entry incompatibility in
599 the case of rVSV-MARV infections on PaKiT01 cell lines.

600 To measure infectivities of rVSVs on each of the cell lines outlined above, so as to
601 calculate the correct viral dose for each MOI, NH_4Cl (20 mM) was added to infected cell
602 cultures at 1–2 hours post-infection to block viral spread, and individual eGFP-positive cells
603 were manually counted at 12–14 hours post-infection.
604
605 *Innate Immune Phenotypes via qPCR of IFN Genes.*
606 Previously published work indicates that immortalized kidney cell lines of *Rousettus*
607 *aegyptiacus* (RoNi/7.1) and *Pteropus alecto* (PaKiT01) exhibit different innate antiviral immune
608 phenotypes through, respectively, induced (Biesold et al. 2011; Pavlovich et al. 2018; Kühl et al.
609 2011; Arnold et al. 2018) and constitutive (Zhou et al. 2016) expression of type I interferon
610 genes. We verified these published phenotypes on our own cell lines infected with rVSV-G,
611 rVSV-EBOV, and rVSV-MARV via qPCR of IFN-α and IFN-β genes across a longitudinal time
612 series of infection.
613 Specifically, we carried out multiple time series of infection of each cell line with each of
614 the viruses described above, under mock infection conditions and at MOIs of 0.0001 and
615 0.001—with the exception of rVSV-MARV on PaKiT01 cell lines, for which infection was only
616 performed at MOI=0.0001 due to limited viral stocks and the extremely low infectivity of this
617 virus on this cell line (thus requiring high viral loads for initial infection). All experiments were
618 run in duplicate on 6-well plates, such that a typical plate for any of the three viruses had two
619 control (mock) wells, two MOI=0.0001 wells and two MOI=0.001 wells, excepting PaKiT01
620 plates, which had two control and four MOI=0.0001 wells at a given time. We justify this
621 PaKiT01 exemption through the expectation that IFN-α expression is constitutive for these cells,

622 and by the assumption that any expression exhibited at the lower MOI should also be present at
623 the higher MOI.

624 For these gene expression time series, four 6-well plates for each cell line–virus
625 combination were incubated with virus for one hour at 37˚C. Following incubation, virus was
626 aspirated off, and cell monolayers were washed in PBS, then covered with an agar plaque assay
627 overlay to mimic conditions under which infection trials were run. Plates were then harvested
628 sequentially at timepoints of roughly 5, 10, 15, and 20 hours post-infection (exact timing varied
629 as multiple trials were running simultaneously). Upon harvest of each plate, agar overlay was
630 removed, and virus was lysed and RNA extracted from cells using the Zymo Quick RNA Mini
631 Prep kit, according to the manufacturer's instructions and including the step for cellular DNA
632 digestion. Post-extraction, RNA quality was verified via nanodrop, and RNA was converted to
633 cDNA using the Invitrogen Superscript III cDNA synthesis kit, according to the manufacturer's
634 instructions. cDNA was then stored at 4˚C and as a frozen stock at -20˚C to await qPCR.

635 We undertook qPCR of cDNA to assess expression of the type I interferon genes, IFN-α
636 and IFN-β, and the housekeeping gene, β-Actin, using primers previously reported in the
637 literature (SI Appendix, Table S3). For qPCR, 2ul of each cDNA sample was incubated with 7ul
638 of deionized water, 1ul of 5UM forward/reverse primer mix and 10ul of iTaq Universal SYBR
639 Green, then cycled on a QuantStudio3 Real-Time PCR machine under the following conditions:
640 initial denaturation at 94˚C for 2 min followed by 40 cycles of: denaturation at 95˚C (5 sec),
641 annealing at 58˚C (15 sec), and extension at 72˚C (10 sec).

642 We report simple δ-Ct values for each run, with raw Ct of the target gene of interest
643 (IFN-α or IFN-β) subtracted from raw Ct of the β-Actin housekeeping gene in SI Appendix,
644 Figure S7. Calculation of fold change upon viral infection in comparison to mock using the δ-δ-

645 Ct method (Livak and Schmittgen 2001) was inappropriate in this case, as we wished to
646 demonstrate constitutive expression of IFN-α in PaKiT01 cells, whereby data from mock cells
647 was identical to that produced from infected cells.
648
649 *Plaque Assays and Time Series Imaging.*
650 After being grown to ~90% confluency, cells were incubated with pelleted rVSVs
651 expressing eGFP (rVSV-G, rVSV-EBOV, rVSV-MARV). Cell lines were challenged with both a
652 low (0.0001) and high (0.001) multiplicity of infection (MOI) for each virus. In a cell monolayer
653 infected at a given MOI (m), the proportion of cells (P), infected by k viral particles can be
654 described by the Poisson distribution: $P(k) = \frac{e^{-m}m^k}{k!}$, such that the number of initially infected
655 cells in an experiment equals: $1 - e^{-m}$. We assumed that a ~90% confluent culture at each
656 trial's origin was comprised of ~$9x10^5$ cells and conducted all experiments at MOIs of 0.0001
657 and 0.001, meaning that we began each trial by introducing virus to, respectively, ~81 or 810
658 cells, representing the state variable 'E' in our theoretical model. Low MOIs were selected to
659 best approximate the dynamics of mean field infection and limit artifacts of spatial structuring,
660 such as premature epidemic extinction when growing plaques collide with plate walls in cell
661 culture.
662 Six well plates were prepared with each infection in duplicate or triplicate, such that a
663 control well (no virus) and 2-3 wells each at MOI 0.001 and 0.0001 were incubated
664 simultaneously on the same plate. In total, we ran between 18-39 trials at each cell-virus-MOI
665 combination, excepting r-VSV-MARV infections on PaKiT01 cells at MOI=0.001, for which we
666 ran only 8 trials due to the low infectivity of this virus on this cell line, which required high viral
667 loads for initial infection. Cells were incubated with virus for one hour at 37˚C. Following

668 incubation, virus was aspirated off, and cell monolayers were washed in PBS, then covered with
669 a molten viscous overlay (50% 2X MEM/L-glutamine; 5% FBS; 3% HEPES; 42% agarose),
670 cooled for 20 minutes, and re-incubated in their original humidified 37˚C, 5% CO_2 environment.
671 After application of the overlay, plates were monitored periodically using an inverted
672 fluorescence microscope until the first signs of GFP expression were witnessed (~6-9.5 hours
673 post-infection, depending on the cell line and virus under investigation). From that time forward,
674 a square subset of the center of each well (comprised of either 64- or 36-subframes and
675 corresponding to roughly 60 and 40% of the entire well space) was imaged periodically, using a
676 CellInsight CX5 High Content Screening (HCS) Platform with a 4X air objective
677 (ThermoFisher, Inc., Waltham, MA). Microscope settings were held standard across all trials,
678 with exposure time fixed at 0.0006 sec for each image. One color channel was imaged, such that
679 images produced show GFP-expressing cells in white and non-GFP-expressing cells in black (SI
680 Appendix, Figure S1).
681 Wells were photographed in rotation, as frequently as possible, from the onset of GFP
682 expression until the time that the majority of cells in the well were surmised to be dead, GFP
683 expression could no longer be detected, or early termination was desired to permit Hoechst
684 staining.
685 In the case of PaKiT01 cells infected with rVSV-EBOV, where an apparently persistent
686 infection established, the assay was terminated after 200+ hours (8+ days) of continuous
687 observation. Upon termination of all trials, cells were fixed in formaldehyde (4% for 15 min),
688 incubated with Hoechst stain (0.0005% for 15 min) (ThermoFisher, Inc., Waltham, MA), then
689 imaged at 4X on the CellInsight CX5 High Content Screening (HCS) Platform. The machine was
690 allowed to find optimal focus for each Hoechst stain image. One color channel was permitted

691 such that images produced showed live nuclei in white and dead cells in black. All original and
692 processed images are freely available for download at the following FigShare repository: DOI:
693 10.6084/m9.figshare.8312807.
694
695 *Hoechst Staining.*
696 Hoechst stain colors cellular DNA, and viral infection is thought to interfere with the
697 clarity of the stain (Dembowski and DeLuca, 2015). As such, infection termination, cell fixation,
698 and Hoechst staining enables generation of a rough time series of uninfectious live cells (i.e.
699 susceptible + antiviral cells) to complement the images which produced time series of
700 proportions infectious. Due to uncertainty over the exact epidemic state of Hoechst-stained cells
701 (*i.e.* exposed but not yet infectious cells may still stain), we elected to fit our models only to the
702 infectious time series derived from GFP-expressing images and used Hoechst stain images as a
703 *post hoc* visual check on our fit only (Figure 5, main text, and SI Appendix, Figures S8-S9).
704
705 *Image Processing.*
706 All image processing and data analysis was carried out in R version 3.6 for MacIntosh (R
707 Core Team 2019). Original images were imported into R and processed via the package
708 EBImage (Pau et al. 2010). Composite images of each well were first split into the 36 or 64-
709 subframes from which they were composed (each subframe represents the visual region of focus
710 for the microscope at the time of imaging). Each subframe was trimmed (to remove border
711 effects), processed individually, and recompiled post-processing into binary form, such that
712 light-colored regions of the original image were assigned a value of 1 (white), and dark regions
713 were assigned a value of 0 (black). In the case of images of GFP-expressing cells, these white

714 regions corresponded to “infectious” cells, while in images of Hoechst-stained nuclei, they
715 indicated live, “uninfected” cells.

716 Microscope focus was poor for control wells and for subframes early in the time series of
717 each trial before GFP expression became apparent, and the original versions of any such
718 subframes were light gray and grainy. Our image processing code identified these subframes as
719 any which possessed a mean pixel value greater than .25 (a value substantially higher than any
720 subframes in which true GFP-expressing or Hoechst-stained cells were visible) and subsequently
721 converted the entire frame to 0 (black).

722 All other subframes were processed following thresholding methods that have been
723 previously described by the authors of EBImage (Pau et al. 2010). As a first pass, all pixels
724 excepting the top 25% lightest pixels tallied were converted to 0 (black). Next, each image frame
725 was walked through a series of secondary thresholding steps using if-else statements in R, such
726 that the lightness threshold for "infectious" status was elevated in frames which were lighter
727 overall due to manual variation in imaging and focusing. Processed subframes were then
728 reconstructed into composite binary images, which were manually checked against original
729 images to ensure consistent and reliable results.

730 Post-processing into binary form, the number of discrete shapes with value of 1 were
731 tabulated within each image, using the max(bwlabel(X)) function in EBimage, to determine a
732 cell count per image, again corresponding to a count of infectious cells for GFP-expressing
733 images and to a count of uninfected cells for Hoechst stain images. All image processing and
734 counting scripts, in addition to the resulting data, are freely available for download at the
735 following FigShare repository: DOI: 10.6084/m9.figshare.8312807.

736

737 *Data processing.*

738 GFP-expressing images were processed and cells counted across the duration of each
739 infection trial, thus generating a time series of infectious cells. For a subset of plates, infection
740 was terminated, and cells were fixed, Hoechst stained, and imaged at periodic intervals across
741 the duration of the time series. Processing of these images thus allowed for construction of a
742 corresponding time series of live, uninfected cells. Because of logistical constraints (i.e. many
743 plates of simultaneously running infection trials and only one available imaging microscope), the
744 time course of imaging across the duration of each trial was quite variable. As such, we fitted a
745 series of statistical models to our raw image data to reconstruct reliable values of the infectious
746 proportion of each well per hour for each distinct trial in all cell line–virus-MOI combinations
747 (SI Appendix, Figure S2-S3).

748 There was considerable natural variation in initial cell counts across each trial, resulting
749 from subtle differences in the seeding density and growth duration of time until the trial was
750 initiated (when wells were subjectively deemed to have reached "90% confluency"). Baseline
751 cell counts were also different across our three cell lines, which varied substantially in natural
752 size. To correct for this variation, we opted to model the proportion of infectious cell spaces per
753 hour for each well, rather than rely on the raw count data. To this end, we collected the
754 maximum number of live cells counted in susceptible control wells at timepoint 0 and set this
755 count to a rough measure of 100% well occupancy for the cell line in question. Using this
756 method, maximum cell counts were, respectively, 103712, 82308, and 92233 for Vero, RoNi/7.1,
757 and PaKiT01 cell lines, reflecting innate variation in cell sizes. We then converted all cell counts
758 tabulated via our image processing code across the infectious time trials into proportions by
759 dividing the counts by the total number of possible cell spaces for the cell line in question.

760 Though clearly subject to some error, these methods nonetheless maintained internal consistency
761 in our counting methods and generated reasonable time series. We originally experimented with
762 directly tabulating the proportion of infected versus uninfected space in our binary images;
763 however, this approach impaired our ability to generalize across more or less densely seeded
764 trials, as well as trials on cell lines of disparate sizes. As such, we adopted the count-to-
765 proportion methods described here.

766 To generate an infectious time series of evenly distributed time steps against which to fit
767 our mean field mechanistic model, we next fit a series of statistical models to the proportional
768 data produced from the image processing methods described above. For the GFP-expressing
769 data, we used the mgcv package in R (Wood 2001) to fit generalized additive models (GAMs) in
770 the Gaussian family, with time elapsed (in hours) post infection as a predictor variable for
771 proportion of infectious cells (the response variable). We fit a separate GAM model to each
772 unique cell – virus – MOI combination, incorporating a random effect of well ID (such that each
773 trial was modeled individually), and we fixed the smoothing parameter at k=7 for all trials, as
774 recommended by the package author (Wood 2001). The gam.predict() function was used to
775 return an estimate of infectious proportions per hour across the duration of each time series for
776 each cell-virus-MOI combination.

777 The uninfected counts from the Hoechst stain data were much less numerous since each
778 count required termination of the infection trial and fixation of cells; by definition, only one data
779 point could be produced per trial. Due to this relative scarcity, we opted to fit a more standard
780 linear regression model, again in the Gaussian family, to these data, rather than using the data-
781 hungry GAM methods employed above. As before, we set time elapsed post infection as the
782 predictor for the Hoechst stain data and produced a unique estimate of the proportion of

783 uninfected cells per hour across the duration of the longest-observed trial. No random effects
784 were included in this model, and the resulting time series were used to estimate natural mortality
785 rates for each cell line, when fit to control well data depicting natural susceptible decline (SI
786 Appendix, Figure S11).
787
788 **Mean Field Model.**
789 *Theoretical Model Details.*
790 To derive the expression for R_0, the basic pathogen reproductive number *in vitro*, we
791 used Next Generation Matrix (NGM) techniques (Diekmann, Heesterbeek, and Metz 1990;
792 Heffernan, Smith, and Wahl 2005), employing Wolfram Mathematica (version 11.2) as an
793 analytical tool (SI Appendix, Text S1). R_0 describes the number of new infections generated by
794 an existing infection in a completely susceptible host population; a pathogen will invade a
795 population when $R_0 > 1$. We then analyzed stability properties of the system, exploring
796 dynamics across a range of parameter spaces, using MatCont (version 2.2) (Dhooge et al. 2008)
797 for Matlab (version R2018a) (SI Appendix, Table S2).
798
799 *Theoretical Model Fitting.*
800 The birth rate, *b,* and natural mortality rate, μ, balance to yield a population-level growth
801 rate, such that it is impossible to estimate both *b* and μ simultaneously from total population size
802 data alone. As such, we fixed *b* at .025 and estimated μ by fitting an infection-absent version of
803 our mean field model to the susceptible time series derived via Hoechst staining of control wells
804 for each of the three cell lines (SI Appendix, Figure S11). This yielded a natural mortality rate, μ,
805 corresponding to a lifespan of approximately 121, 191, and 84 hours, respectively, for Vero,

806 RoNi/7.1, and PaKiT01 cell lines (SI Appendix, Figure S11). We then fixed the virus incubation
807 rate, σ, as the inverse of the shortest observed duration of time from initial infection to the
808 observation of the first infectious cells via fluorescent microscope for all nine cell line – virus
809 combinations (ranging 6 to 9.5 hours). We fixed α, the infection-induced mortality rate, at $\frac{1}{6}$, an
810 accepted standard for general viral kinetics (Howat et al. 2006), and held *c,* the rate of antiviral
811 cell regression to susceptible status, at 0 for the timespan (<200 hours) of the experimental cell
812 line infection trials.

813 We estimated cell line–virus-MOI-specific values for β, ρ, and ε by fitting the
814 deterministic output of infectious proportions in our mean field model to the full suite of
815 statistical outputs of all trials for each infected cell culture time series (SI Appendix, Figure S4-
816 S5). Fitting was performed by minimizing the sum of squared differences between the
817 deterministic model output and cell line–virus-MOI-specific infectious proportion of the data at
818 each timestep. We optimized parameters for MOI = 0.001 and 0.0001 simultaneously to leverage
819 statistical power across the two datasets, estimating a different transmission rate, β, for trials run
820 at each infectious dose but, where applicable, estimating the same rates of ρ and ε across the two
821 time series. We used the differential equation solver lsoda() in the R package deSolve (Soetaert,
822 Petzoldt, and Setzer 2010) to obtain numerical solutions for the mean field model and carried out
823 minimization using the 'Nelder-Mead' algorithm of the optim() function in base R. All model
824 fits were conducted using consistent starting guesses for the parameters, β (β= 3), and where
825 applicable, ρ (ρ = 0.001) and ε (ε = 0.001). In the case of failed fits or indefinite hessians, we
826 generated a series of random guesses around the starting conditions and continued estimation
827 until successful fits were achieved.

828 All eighteen cell line–virus-MOI combinations of data were fit by an immune absent ($\varepsilon =$
829 $\rho = 0$) version of the theoretical model and, subsequently, an induced immunity ($\varepsilon = 0$; $\rho > 0$)
830 and constitutive immunity ($\varepsilon > 0$; $\rho > 0$) version of the model. Finally, we compared fits across
831 each cell line–virus-MOI combination via AIC. In calculating AIC, the number of fitted
832 parameters in each model (k) varied across the immune phenotypes, with one parameter (β)
833 estimated for absent immune assumptions, two (β and ρ) for induced immune assumptions, and
834 three (β, ρ, and ε) for constitutive immune assumptions. The sample size (n) corresponded to the
835 number of discrete time steps across all empirical infectious trials to which the model was fitted
836 for each cell-line virus combination. All fitting and model comparison script is freely available
837 for download at the following FigShare repository: DOI: 685 10.6084/m9.figshare.8312807.
838
839 *Spatial Model Simulations.*
840 Finally, we verified all mean field fits in a spatial context, in order to more thoroughly
841 elucidate the role of antiviral cells in each time series. We constructed our spatial model in C++
842 implemented in R using the packages Rcpp and RcppArmadillo (Eddelbuettel and Francois
843 2011; Eddelbuettel and Sanderson 2017). Following Nagai and Honda (2001) and Howat et al.
844 (2006), we modeled this system on a two-dimensional hexagonal lattice, using a ten-minute
845 epidemic timestep for cell state transitions. At the initialization of each simulation, we randomly
846 assigned a duration of natural lifespan, incubation period, infectivity period, and time from
847 antiviral to susceptible status to all cells in a theoretical monolayer. Parameter durations were
848 drawn from a normal distribution centered at the inverse of the respective fixed rates of μ, σ, α,
849 and c, as reported with our mean field model. These durations were updated iteratively with each
850 time-step, based on each cell's epidemic status. We fixed the parameters for antiviral acquisition

851 (ε and ρ) at those values estimated in the mean field model, and to compensate for a higher virus
852 invasion threshold under spatial conditions, we fixed the birth rate *b* and the cell-to-cell
853 transmission rate, β, at ten times the values recovered from optimization of the mean field model
854 (SI Appendix, Table S1).

855 Transitions involving the birth rate (*b*), the transmission rate (β), and the induced (ρ) and
856 constitutive (ε) rates of antiviral acquisition were governed probabilistically and adjusted
857 dynamically based on each cell's local and global environment. The birth rate, b, was thus
858 multiplied by the proportion of susceptible cells within a six neighbor radius of a focal dead cell,
859 while β was multiplied by the proportion of infectious cells within a thirty-six neighbor radius of
860 a focal susceptible cell; both ρ and ε were multiplied by the global proportion of, respectively,
861 exposed and susceptible cells at a given time-step. We then simulated ten stochastic spatial time
862 series for all cell-virus combinations under all three immune assumptions at a population size of
863 10,000 cels and compared model output with data in SI Appendix, Figure S10. Spatial model
864 code is available for public access at the following FigShare repository: DOI:
865 10.6084/m9.figshare.8312807.
866
867

Acknowledgments

CEB was supported by a National Science Foundation Graduate Research Fellowship at Princeton University and a Miller Institute for Basic Research Fellowship at UC Berkeley. Tissue culture experiments were funded by an NIH grant R01 AI134824 to KC. Work in LFW's lab was funded by the Singapore National Research Foundation grants (NRF2012NRF-CRP001-056 and NRF2016NRF-NSFC002-013). CD was supported by the German Research Council (DFG) grant DFG SPP1596 (DR 772/10–2), the Federal Ministry of Education and Research (BMBF) grant RAPID (#01KI1723A) and the EU Horizon 2020 grant EVAg (#653316). The authors thank the Chandran lab at Albert Einstein College of Medicine – in particular, Cecilia Harold, Megan Slough, Rohit Jangra, and Tanwee Alkutkar – for technical support during tissue culture experiments. The authors further thank Jessica Metcalf and the Graham lab at Princeton for conceptual guidance throughout the project's development.

891 **References**

892 Ahn, Matae, Danielle E. Anderson, Qian Zhang, Chee Wah Tan, Beng Lee Lim, Katarina Luko,
893 Ming Wen, et al. 2019. "Dampened NLRP3-Mediated Inflammation in Bats and
894 Implications for a Special Viral Reservoir Host." *Nature Microbiology* 4: 789–99.
895 https://doi.org/10.1038/s41564-019-0371-3.

896 Arnold, Catherine E, Jonathan C Guito, Louis A Altamura, Sean P Lovett, Elyse R Nagle,
897 Gustavo F Palacios, and Mariano Sanchez-lockhart. 2018. "Transcriptomics Reveal
898 Antiviral Gene Induction in the Egyptian Rousette Bat Is Antagonized in Vitro by Marburg
899 Virus Infection." *Viruses* 10 (607). https://doi.org/10.3390/v10110607.

900 Baccam, Prasith, Catherine Beauchemin, Catherine A Macken, Frederick G Hayden, and Alan S
901 Perelson. 2006. "Kinetics of Influenza A Virus Infection in Humans." *Journal of Virology*
902 80 (15): 7590–99. https://doi.org/10.1128/JVI.01623-05.

903 Biesold, Susanne E., Daniel Ritz, Florian Gloza-Rausch, Robert Wollny, Jan Felix Drexler,
904 Victor M. Corman, Elisabeth K V Kalko, Samuel Oppong, Christian Drosten, and Marcel
905 A. Müller. 2011. "Type I Interferon Reaction to Viral Infection in Interferon-Competent,
906 Immortalized Cell Lines from the African Fruit Bat Eidolon Helvum." *PLoS ONE* 6 (11).
907 https://doi.org/10.1371/journal.pone.0028131.

908 Bonhoeffer, S., R. M. May, G. M. Shaw, and M. A. Nowak. 1997. "Virus Dynamics and Drug
909 Therapy." *Proceedings of the National Academy of Sciences* 94 (13): 6971–76.
910 https://doi.org/10.1073/pnas.94.13.6971.

911 Brook, Cara E., and Andrew P. Dobson. 2015. "Bats as 'special' Reservoirs for Emerging
912 Zoonotic Pathogens." *Trends in Microbiology* 23 (3): 172–80.
913 https://doi.org/10.1016/j.tim.2014.12.004.

914 Brook, Cara E., Hafaliana Christian Ranaivoson, Christopher C. Broder, Andrew A.
915 Cunningham, Jean-Michel Héraud, Alison J. Peel, Louise Gibson, James L.N. Wood, C.
916 Jessica Metcalf, and Andrew P. Dobson. 2019. "Disentangling Serology to Elucidate
917 Henipa- and Filovirus Transmission in Madagascar Fruit Bats." *Journal of Animal Ecology*
918 00: 1– 16. https://doi.org/10.1111/1365-2656.12985.
919 Calisher, Charles H, James E Childs, Hume E Field, Kathryn V Holmes, and Tony Schountz.
920 2006. "Bats: Important Reservoir Hosts of Emerging Viruses." *Clinical Microbiology*
921 *Reviews* 19 (3): 531–45. https://doi.org/10.1128/CMR.00017-06.
922 Coffin, John M. 1995. "HIV Population Dynamics in Vivo: Implications for Genetic Variation,
923 Pathogenesis, and Therapy." *Science (New York, N.Y.)* 267 (5197): 483–89.
924 Crameri, Gary, Shawn Todd, Samantha Grimley, Jennifer A. McEachern, Glenn A. Marsh, Craig
925 Smith, Mary Tachedjian, et al. 2009. "Establishment, Immortalisation and Characterisation
926 of Pteropid Bat Cell Lines." *PLoS ONE* 4 (12): e8266.
927 https://doi.org/10.1371/journal.pone.0008266.
928 Desmyter, J, J L Melnick, and W E Rawls. 1968. "Defectiveness of Interferon Production and of
929 Rubella Virus Interference in a Line of African Green Monkey Kidney Cells (Vero)."
930 *Journal of Virology* 2 (10): 955–61. https://doi.org/J. Virol. 1968 2:1955.
931 Dhooge, A., W. Govaerts, Yu A. Kuznetsov, H. G E Meijer, and B. Sautois. 2008. "New
932 Features of the Software MatCont for Bifurcation Analysis of Dynamical Systems."
933 *Mathematical and Computer Modelling of Dynamical Systems* 14 (2): 147–75.
934 https://doi.org/10.1080/13873950701742754.
935 Diekmann, O., J.A.P. Heesterbeek, and J.A.J Metz. 1990. "On the Definition and Computation of
936 the Basic Reproduction Ratio R0 in Models for Infectious Diseases in Heterogenous

Populations." *Journal of Mathematical Biology* 28: 365–82.

Eddelbuettel, Dirk, and Romain Francois. 2011. "Rcpp: Seamless R and C++ Integration." *Journal of Statistical Software* 40: 1–18. https://doi.org/10.1007/978-1-4614-6868-4.

Eddelbuettel, Dirk, and Conrad Sanderson. 2017. "RcppArmadillo: Accelerating R with High-Performance C++ Linear Algebra." *Computational Statistics and Data Analysis* 71 (2014): 1–16.

Emeny, J. M., and M. J. Morgan. 1979. "Regulation of the Interferon System: Evidence That Vero Cells Have a Genetic Defect in Interferon Production." *Journal of General Virology* 43 (1): 247–52. https://doi.org/10.1099/0022-1317-43-1-247.

Emery, V.C., A.V. Cope, E.F. Bowen, D. Gor, and P.D. Griffiths. 1999. "The Dynamics of Human Cytomegalovirus Replication in Vivo." *The Journal of Experimental Medicine* 190 (2): 177–82. https://doi.org/10.1084/jem.190.2.177.

Haydon, Daniel T, Sarah Cleaveland, Louise H Taylor, and M Karen Laurenson. 2002. "Identifying Reservoirs of Infection: A Conceptual and Practical Challenge." *Emerging Infectious Diseases* 8 (12): 1468–73. https://doi.org/10.3201/eid0812.010317.

Heffernan, J.M., R.J. Smith, and L.M. Wahl. 2005. "Perspectives on the Basic Reproductive Ratio." *Journal of The Royal Society Interface* 2 (4): 281–93. https://doi.org/10.1098/rsif.2005.0042.

Ho, David D., Avidan U. Neumann, Alan S. Perelson, Wen Chen, John M. Leonard, and Martin Markowitz. 1995. "Rapid Turnover of Plasma Virions and CD4 Lymphocytes in HIV-1 Infection." *Nature* 373: 123–26. https://doi.org/10.1038/373123a0.

Hooper, Peter, Sherif Zaki, Peter Daniels, and Deborah Middleton. 2001. "Comparative Pathology of the Diseases Caused by Hendra and Nipah Viruses." *Microbes and Infection* 3

960 (4): 315–22. https://doi.org/10.1016/S1286-4579(01)01385-5.

961 Howat, Tom J, Cristina Barreca, Peter O'Hare, Julia R Gog, and Bryan T Grenfell. 2006.
962 "Modelling Dynamics of the Type I Interferon Response to in Vitro Viral Infection."
963 *Journal of the Royal Society, Interface* 3 (10): 699–709.
964 https://doi.org/10.1098/rsif.2006.0136.

965 Kacprzyk, Joanna, Graham M. Hughes, Eva M. Palsson-McDermott, Susan R. Quinn, Sébastien
966 J. Puechmaille, Luke A. J. O'Neill, and Emma C. Teeling. 2017. "A Potent Anti-
967 Inflammatory Response in Bat Macrophages May Be Linked to Extended Longevity and
968 Viral Tolerance." *Acta Chiropterologica* 19 (2): 219–28.
969 https://doi.org/10.3161/15081109ACC2017.19.2.001.

970 Keeling, Matt J., and Pejman Rohani. 2008. *Modeling Infectious Diseases in Humans and*
971 *Animals.* Princeton, NJ: Princeton University Press.

972 Kühl, Annika, Markus Hoffmann, Marcel A. Müller, Vincent J. Munster, Kerstin Gnirß, Miriam
973 Kiene, Theodros Solomon Tsegaye, et al. 2011. "Comparative Analysis of Ebola Virus
974 Glycoprotein Interactions with Human and Bat Cells." *Journal of Infectious Diseases* 204:
975 S840–S849. https://doi.org/10.1093/infdis/jir306.

976 Kuzmin, I.V., Toni M. Schwarz, Philipp A. Ilinykh, Ingo Jordan, Thamas G. Ksiazek, Ravi
977 Sachidanandam, Christopher F. Basler, and Alexander Bukreyev. 2017. "Innate Immune
978 Response of Bat and Human Cells to Filoviruses: Commonalities and Distinctions." *Journal*
979 *of Virology* 91 (8): e02471-16. https://doi.org/10.1128/JVI.02471-16.

980 Livak, K J, and T D Schmittgen. 2001. "Analysis of Relative Gene Expression Data Using Real-
981 Time Quantitative PCR and the 2^(-ΔΔCT) Method." *Methods* 25 (4): 402–8.
982 https://doi.org/10.1006/meth.2001.1262.

983 Mahanty, Siddhartha, and Mike Bray. 2004. "Pathogenesis of Filoviral Haemorrhagic Fevers."
984 *Lancet Infectious Diseases* 4 (8): 487–98. https://doi.org/10.1016/S1473-3099(04)01103-X.
985 Miller, Emily Happy, Gregor Obernosterer, Matthijs Raaben, Andrew S Herbert, Maika S
986 Deffieu, Anuja Krishnan, Esther Ndungo, et al. 2012. "Ebola Virus Entry Requires the
987 Host-Programmed Recognition of an Intracellular Receptor." *The EMBO Journal* 31 (8):
988 1947–60. https://doi.org/10.1038/emboj.2012.53.
989 Morris, Sinead E., Andrew J. Yates, Rik L. de Stwart, Rory D. de Vries, Michael J. Mina, Ashley
990 N. Nelson, Wen-Hsuan W. Lin, Roger D. Kouyos, Diane E. Griffin, and Bryan T. Grenfell.
991 2018. "Modeling the Measles Paradox Reveals the Importance of Cellular Immunity in
992 Regulating Viral Clearance." *PLoS Pathogens* 14 (12): e1007493.
993 Neumann, AU, NP Lam, H Dahari, DR Gretch, TE Wiley, TJ Layden, and AS Perelson. 1998.
994 "Hepatitis C Viral Dynamics in Vivo and the Antiviral Efficacy of Interferon-Alpha
995 Therapy." *Science (New York, N.Y.)* 282: 103–7.
996 Ng, Melinda, and Kartik Chandran. 2018. "Unpublished Results."
997 Ng, Melinda, Esther Ndungo, Maryska Kaczmarek, Andrew S. Herbert, Tabea Binger, Rebekah
998 James, Rohit K. Jangra, et al. 2015. "NPC1 Contributes to Species-Specific Patterns of
999 Ebola Virus Infection in Bats." *ELife* 4: e11785. https://doi.org/10.7554/eLife.11785.
1000 Nicholls, J M, L L Poon, K C Lee, W F Ng, S T Lai, C Y Leung, C M Chu, et al. 2003. "Lung
1001 Pathogy of Fatal Severe Acute Respiratory Syndrom." *Lancet* 361: 1773–78.
1002 https://doi.org/10.1016/S0140-6736(03)13413-7.
1003 Nowak, M. A., and R. M. May. 2000. *Virus Dynamics: Mathematical Principles of Immunology*
1004 *and Virology*. Oxford, UK: Oxford University Press.
1005 Nowak, Martin A., Robert M. May, Rodney E. Phillips, Sarah Rowland-Jones, David G. Lalloo,

1006 Steven McAdam, Paul Klenerman, et al. 1995. “Antigenic Oscillations and Shifting
1007 Immunodominance in HIV-1 Infections.” *Nature* 375: 606–11.
1008 Nowak, Martin A, Sebastian Bonhoeffer, Andrew M Hill, Richard Boehme, Howard C Thomas,
1009 and Hugh McDade. 1996. “Viral Dynamics in Hepatitis B Virus Infection.” *Proceedings of*
1010 *the National Academy of Sciences* 93: 4398–4402.
1011 http://www.pnas.org/content/pnas/93/9/4398.full.pdf.
1012 Pau, Gregoire, Florian Fuchs, Oleg Sklyar, Michael Boutros, and Wolfgang Huber. 2010.
1013 “EBImage-an R Package for Image Processing with Applications to Cellular Phenotypes.”
1014 *Bioinformatics* 26 (7): 979–81. https://doi.org/10.1093/bioinformatics/btq046.
1015 Pavlovich, Stephanie S., Sean P. Lovett, Galina Koroleva, Jonathan C. Guito, Catherine E.
1016 Arnold, Elyse R. Nagle, Kirsten Kulcsar, et al. 2018. “The Egyptian Rousette Genome
1017 Reveals Unexpected Features of Bat Antiviral Immunity.” *Cell* 173 (5): 1098–1110.
1018 https://doi.org/10.1016/j.cell.2018.03.070.
1019 Pawelek, Kasia A., Giao T. Huynh, Michelle Quinlivan, Ann Cullinane, Libin Rong, and Alan S.
1020 Perelson. 2012. “Modeling Within-Host Dynamics of Influenza Virus Infection Including
1021 Immune Responses.” *PLoS Computational Biology* 8 (6): e1002588.
1022 https://doi.org/10.1371/journal.pcbi.1002588.
1023 Peel, Alison J., Kate S. Baker, David T. S. Hayman, Christopher C. Broder, Andrew A.
1024 Cunningham, Anthony R. Fooks, Romain Garnier, James L. N. Wood, and Olivier Restif.
1025 2018. “Support for Viral Persistence in Bats from Age-Specific Serology and Models of
1026 Maternal Immunity.” *Scientific Reports* 8 (1): 3859. https://doi.org/10.1038/s41598-018-
1027 22236-6.
1028 Peel, Alison J, Kate S Baker, Gary Crameri, Jennifer A Barr, David TS Hayman, Edward

1029 Wright, Christopher C Broder, et al. 2012. “Henipavirus Neutralising Antibodies in an
1030 Isolated Island Population of African Fruit Bats.” *PloS One* 7 (1): e30346.
1031 https://doi.org/10.1371/journal.pone.0030346.
1032 Perelson, A S, A U Neumann, M Markowitz, J M Leonard, and D D Ho. 1996. “HIV-1
1033 Dynamics in Vivo: Virion Clearance Rate, Infected Cell Life-Span, and Viral Generation
1034 Time.” *Science (New York, N.Y.)* 271 (5255): 1582–86.
1035 https://doi.org/10.1126/science.271.5255.1582.
1036 Perelson, Alan S. 2002. “Modelling Viral and Immune System Dynamics.” *Nature Reviews*
1037 *Immunology* 2 (1): 28–36. https://doi.org/10.1038/nri700.
1038 Plowright, Raina K., Alison J. Peel, Daniel G. Streicker, Amy Gilbert, Hamish McCallum, James
1039 Wood, Michelle L. Baker, and Olivier Restif. 2016. “Transmission or Within-Host
1040 Dynamics Driving Pulses of Zoonotic Viruses in Reservoir-Host Populations.” *PLoS*
1041 *Neglected Tropical Diseases* 10 (8): e0004796.
1042 https://doi.org/10.1371/journal.pntd.0004796.
1043 Radke, K L, C Colby, J R Kates, H M Krider, and D M Prescott. 1974. “Establishment and
1044 Maintenance of the Interferon-Induced Antiviral State: Studies in Enucleated Cells.”
1045 *Journal of Virology* 13 (3): 623–30.
1046 http://www.ncbi.nlm.nih.gov/pubmed/4362865%0Ahttp://www.pubmedcentral.nih.gov/arti
1047 clerender.fcgi?artid=PMC355347.
1048 Rasmussen, L., and L. B. Farley. 1975. “Inhibition of *Herpesvirus Hominis* Replication by
1049 Human Interferon.” *Infection and Immunity* 12 (1): 104–8.
1050 Rhim, J. S., K. Schell, B. Creasy, and W. Case. 1969. “Biological Characteristics and Viral
1051 Susceptibility of an African Green Monkey Kidney Cell Line (Vero).” *Proceedings of the*

Society for Experimental Biology and Medicine 132 (2): 670-678.

Saenz, Roberto A, Michelle Quinlivan, Debra Elton, Shona MacRae, Anthony S Blunden, Jennifer A Mumford, Janet M Daly, et al. 2010. "Dynamics of Influenza Virus Infection and Pathology." *Journal of Virology* 84 (8): 3974–83. https://doi.org/10.1128/JVI.02078-09.

Samuel, C. E., and G. S. Knutson. 1982. "Mechanism of Interferon Action." *Journal of Biological Chemistry* 257 (19): 11791–95.

Schountz, Tony, Michelle L Baker, John Butler, and Vincent Munster. 2017. "Immunological Control of Viral Infections in Bats and the Emergence of Viruses Highly Pathogenic to Humans." *Frontiers in Immunology* 8 (September): Article 1098. https://doi.org/10.3389/fimmu.2017.01098.

Soetaert, Karline, Thomas Petzoldt, and R Woodrow Setzer. 2010. "Package DeSolve: Solving Initial Value Differential Equations in R." *Journal of Statistical Software* 33 (9): 1–25. https://doi.org/10.18637/jss.v033.i09.

Stetson, Daniel B., and Ruslan Medzhitov. 2006. "Type I Interferons in Host Defense." *Immunity* 25 (3): 373–81. https://doi.org/10.1016/j.immuni.2006.08.007.

Team, R Core. 2019. "R: A Language and Environment for Statistical Computing." *R Foundation for Statistical Computing*. Vienna, Austria.

Wang, Lin-Fa, and Danielle E Anderson. 2019. "Viruses in Bats and Potential Spillover to Animals and Humans." *Current Opinion in Virology* 34: 79–89. https://doi.org/10.1016/j.coviro.2018.12.007.

Webb, Steven D., Matt J. Keeling, and Mike Boots. 2007. "Host-Parasite Interactions between the Local and the Mean-Field: How and When Does Spatial Population Structure Matter?" *Journal of Theoretical Biology* 249 (1): 140–52. https://doi.org/10.1016/j.jtbi.2007.06.013.

1075 Wong, Anthony C, Rohini G Sandesara, Nirupama Mulherkar, Sean P Whelan, and Kartik
1076 Chandran. 2010. "A Forward Genetic Strategy Reveals Destabilizing Mutations in the
1077 Ebolavirus Glycoprotein That Alter Its Protease Dependence during Cell Entry." *Journal of*
1078 *Virology* 84 (1): 163–75. https://doi.org/10.1128/JVI.01832-09.
1079 Wood, Simon N. 2001. "Mgcv: GAMs and Generalized Ridge Regression for R." *R News* 1/2:
1080 20–24.
1081 Xie, Jiazheng, Yang Li, Xurui Shen, Jiazheng Xie, Yang Li, Xurui Shen, Geraldine Goh, et al.
1082 2018. "Dampened STING-Dependent Interferon Activation in Bats." *Cell Host and*
1083 *Microbe* 23: 297–301.
1084 Zhang, Guojie, Christopher Cowled, Zhengli Shi, Zhiyong Huang, Kimberly a Bishop-Lilly,
1085 Xiaodong Fang, James W Wynne, et al. 2013. "Comparative Analysis of Bat Genomes
1086 Provides Insight into the Evolution of Flight and Immunity." *Science (New York, N.Y.)* 339
1087 (6118): 456–60. https://doi.org/10.1126/science.1230835.
1088 Zhou, Peng, Mary Tachedjian, James W Wynne, Victoria Boyd, Jie Cui, Ina Smith, Christopher
1089 Cowled, et al. 2016. "Contraction of the Type I IFN Locus and Unusual Constitutive
1090 Expression of IFN-α in Bats." *Proceedings of the National Academy of Sciences* 113 (10):
1091 2696–2701. https://doi.org/10.1073/pnas.1518240113.
1092
1093